


2012

# Microscale platform technologies for biomimetics and biomedical engineering

Ji Won Lee  
*Iowa State University*

Follow this and additional works at: <https://lib.dr.iastate.edu/etd>

 Part of the [Biomedical Commons](#), and the [Electrical and Electronics Commons](#)

## Recommended Citation

Lee, Ji Won, "Microscale platform technologies for biomimetics and biomedical engineering" (2012). *Graduate Theses and Dissertations*. 12685.  
<https://lib.dr.iastate.edu/etd/12685>

This Dissertation is brought to you for free and open access by the Iowa State University Capstones, Theses and Dissertations at Iowa State University Digital Repository. It has been accepted for inclusion in Graduate Theses and Dissertations by an authorized administrator of Iowa State University Digital Repository. For more information, please contact [digirep@iastate.edu](mailto:digirep@iastate.edu).

**Microscale platform technologies for biomimetics and biomedical engineering**

by

**Ji Won Lee**

A dissertation to the graduate faculty

in partial fulfillment of the requirements for the degree of

**DOCTOR OF PHILOSOPHY**

Major: Electrical Engineering

Program of Study Committee:  
Jaeyoun Kim, Major Professor

Robert J. Weber

Mani Mina

Liang Dong

Santosh Pandey

Iowa State University

Ames, Iowa

2012

Copyright © Ji Won Lee, 2012, All rights reserved.

**TABLE OF CONTENTS**

<b>LIST OF FIGURES</b>	vi
<b>LIST OF TABLES</b>	xi
<b>ACKNOWLEDGEMENTS</b>	xii
<b>ABSTRACT</b>	xiii
<b>CHAPTER 1. Introduction</b>	
1.1 Research Motivations	1
1.1.1 Biomedical engineering	1
1.1.2 Biomimetics	3
1.2 Overview of current technologies	5
1.2.1 Microfluidics and Microfabrication	5
1.2.2 Soft lithography and Polymer MEMS	6
1.3 Challenges	8
1.3.1 Miniaturization	8
1.3.2 Cost deduction	9
1.3.3 Easy fabrication	9
1.4 Approaches	9
1.5 Thesis Organizations	11
1.6 References	12

## **CHAPTER 2. Two-dimensional optofluidic liquid-core waveguiding based on optimized integration of single- and multiple-layer ARROWs**

2.1 Abstract	16
2.2 Introduction	16
2.3 Theoretical Backgrounds	19
2.4 Design and Validation	22
2.4.1 Model Structure Design	22
2.4.2 Numerical Validation	25
2.4.3 Optimization and Application	27
2.4.4 Impact of Structural Parameters	30
2.4.5 Dual-Use of SL-ARROW	31
2.5 Conclusion	32
2.6 Acknowledgement	33
2.7 References	33

## **CHAPTER 3. Fabrication of strongly anchored, ultrahigh aspect-ratio elastomeric microwires for mechanical and optical applications**

3.1 Abstract	36
3.2 Introduction	36
3.3 Fabrication Principle and Details	38
3.4 Structural Characteristics	42
3.5 Tensile Properties	46

3.6 Optical Properties and Application	48
3.7 Conclusion	51
3.8 Acknowledgement	51
3.9 References	51

#### **CHAPTER 4. Compact range-tunable gas flow sensor utilizing stretchable optical microwire**

4.1 Abstract	54
4.2 Introduction	54
4.3 Fabrication Details	55
4.4 Basic Principles	56
4.5 Structural Characteristics	59
4.6 Experimental Results	61
4.7 Conclusion	62
4.8 Acknowledgement	63
4.9 References	63

#### **CHAPTER 5. Sucrose-based fabrication of 3D-networked, cylindrical microfluidic channel for rapid-prototyping of lab-on-a-chip and vaso-mimetic device**

5.1 Abstract	66
5.2 Introduction	66
5.3 Materials and Methods	69
5.3.1 Pulling and shaping of sucrose fiber templates	69

5.3.2 Sucrose template bonding, assembly, and replication	71
5.4 Results and Discussion	72
5.4.1 Physical characteristics of sucrose templates	72
5.4.2 MF junction formation	73
5.4.3 3D MF channels trajectories and internal looping	75
5.4.4 Vaso-mimetic architectures: tapered junctions and stenosis	75
5.5 Conclusion	77
5.6 Acknowledgement	77
5.7 Notes and References	77
<b>CHAPTER 6. Conclusion and Future Aspects</b>	<b>81</b>

## LIST OF FIGURES

- Figure 1.1 (a) Healthy and infected red blood cells (RBCs) show different levels of stiffness and trapping probability in the capillaries, (b) Vasomimetic structure and its microscopic view to give biomedical technology examples. 2
- Figure 1.2 (a) Artificial compound eyes and (b) an artificial hair cell to show well-known biomimetic examples. 3
- Figure 1.3 Summary of biomimetic sensors which states its popularities and on-going researches in different disciplines. 4
- Figure 1.4 Chip based 16 nanoliter bioreactors for bacteria which illustrate one of the microfluidic applications. 5
- Figure 1.5 Four kinds of Soft lithography depending on the fabrication methods (a) step and flash (b) replica molding (c) microtransfer molding (d) micromolding in capillaries. 7
- Figure 2.1 The proposed liquid-core waveguide that integrates the single layer (SL)- and multiple layer (ML)-ARROWs. The SL-ARROWs also function as the microfluidic channel walls and the spacer which separates the two ML-ARROWs. 18
- Figure 2.2 The ray model for the lateral confinement configuration based on the SL-ARROW/Liquid-Core/SL-ARROW structure.  $n_S > n_c > n_a$  is assumed. 20
- Figure 2.3 (a) The dotted and solid curves show the calculated values of  $L_{prop,vert}$ , the propagation distance owing only to the 1D ML-ARROW confinement, and  $L_{prop,2D}$ , the combined result of ML/SL-ARROWs. Vertical bars mark the wavelengths at which the lateral confinement due to the SL-ARROW fails. (b) The curve shows the relation between the liquid-core width  $w$  and the real part of  $n_{eff,lat}$ , 23

the effective index arising from the SL-ARROW-based lateral confinement, calculated by EIM/TMM. As the liquid-core widens,  $n_{eff,lat}$  increases monotonically, approaching the target value of  $n_{eff,vert}$ . (c) Unlike the monotonic increase in  $\text{Re}\{n_{eff,lat}\}$ ,  $L_{prop,2D}$  increases with substantial fluctuations as  $w$  widens. The arrows specify the values of  $w$  at which the condition of Eq. (8) is satisfied.

Figure 2.4 (a) Comparison of EIM/TMM and 2D vectorial FEM results. (b) Calculated profiles of the 2D LCW's fundamental mode at two different  $\lambda_o$  marked in Fig. 2.3(a). 26

Figure 2.5 (a)  $L_{prop,2D}$  curve as a function of  $\lambda_o$  when  $d_s$  was increased to 3.3  $\mu\text{m}$ . The vertical bars mark the new  $\lambda_o$  values at which the SL-ARROW-based lateral confinement fails. The  $L_{prop,2D}$  curve for  $d_s = 3.0 \mu\text{m}$  is also superimposed for comparison. It indicates that the increase in  $d_s$  red-shifts the  $L_{prop,2D}$  dips, making the  $L_{prop,2D}$  profile single-peaked near  $\lambda_o \sim 750 \text{ nm}$ . (b)  $L_{prop,2D}$  curve for a ML/SL-ARROW for which  $d_s$  and  $w$  were maintained at 3.0 and 9.0  $\mu\text{m}$  but  $h$  was increased to 3.3  $\mu\text{m}$ . The increase in the vertical confinement itself has led to an augmented  $L_{prop,2D}$ . (c) Another  $L_{prop,2D}$  curve for a ML/SL-ARROW designed for the optofluidic excitation and detection of Alexa Fluor 546 dye. 28

Figure 2.6 (a) The calculated profile of the mode supported by the SL-ARROW ridge. (b) The decay of  $|\mathbf{E}|$  into the liquid-core. 32

Figure 3.1 The process flow for the fabrication of monolithically anchored elastomeric microwires: (a) Preparation of a patterned array of wire-templates, (b–e) The first replication to make a transition mold, (f–g) The second replication with PDMS, and (h–i) Release and testing of the microwire's tensile characteristics. 39

Figure 3.2 (a) A  $10 \times 10$  array of 150  $\mu\text{m}$ -diameter, 2.5 mm-long doubly-anchored 42



PDMS microwires. (b) The microwires exhibit excellent lightpipe characteristics. (c) When stretched by a pair of tweezers, the microwires withstood  $>300\%$  elongation.

Figure 3.3 Microscope images of a  $170\ \mu\text{m}$ -diameter,  $2.5\ \text{mm}$ -long microwire (a) before and (b) during a  $440\%$  elongation. (c) A further magnified image of the anchoring site under stretching (the circled area in (b)). 43

Figure 3.4 SEM images of a microwire (a) before ( $181\ \mu\text{m}$  at the waist) and (b) during a  $300\%$  elongation ( $118\ \mu\text{m}$  at the waist). (c) The surface of the same microwire after 25 cycles of  $300\%$  elongations. The inset of (a) shows the surface quality at a higher magnification. 44

Figure 3.5 AFM images obtained by scanning over a  $16\ \mu\text{m}^2$  area of the surface of a PDMS microwire (a) before and (b) after 25 cycles of  $400\%$  stretching. 45

Figure 3.6 The force-strain curves of the four characterized microwires. The symbols represent the measurements and the super-imposed curves show the results of curve-fitting to the Ogden model. 46

Figure 3.7 (a) Optical throughput measured as the length of the PDMS microwire is being increased by elongation  $\Delta l$ . The dotted curve represents the result of curve-fitting to exponential decay. (b) The optical throughput from a  $2\ \text{cm}$ -long,  $184\ \mu\text{m}$ -diameter PDMS microwire as a function of the radius of curvature. The inset describes the experimental setup and the parameters schematically. The insets also show the microwires bent with different  $R$  values. The red-colored microwires carry the HeNe light. (c) The same microwire was used as a jump-wire optically connecting a surface-mounted LED to a spot on the circuit board. 49

Figure 4.1 (a)-(e) PDMS microwire fabrication steps: (a)-(b) Preparation of a 56

water-soluble wax mold with a cylindrical hole, (c)-(d) Inject liquid phase-PDMS through the hole, (e) After solidification, the microwire is released by water bath. (f) and (g) show images of a microwire (radius: 100  $\mu\text{m}$ , length: 1.2 cm), monolithically attached to handling pads at both ends, in its normal and 200% elongated states, respectively.

Figure 4.2 Operational principle of stretchable optical microwire-based gas flow sensing: The aperture translates the flow-induced bending into a decrease in the output power as a function of  $d$ , the center-to-center displacement between the beam and the aperture. 57

Figure 4.3 Experimental setup for gas flow sensing based on the stretchable optical microwire. The microwire is to be stretched by the linear translation stage on which all the components from the fixture to the detection head are mounted. 58

Figure 4.4 (a) Measured output power as a function of the gas flow rate and elongation. Spline-interpolation lines are added for visual aid. (b) The results of fitting the curves of (a) into Eq. 1. The inset shows the transducer model and parameters. 60

Figure 5.1 Schematic outline of the sucrose-based rapid-prototyping process: (a) We melted sucrose and (b) pulled fibers which can be (c) shaped and (d) bonded with water-based adhesives (e) to form a template assembly. (f) Then we immersed it in liquid-phase PDMS. (g) Upon curing, the template was removed with water bath. For visualization, we filled the channels with dye. (h) A 3D MF channel in PDMS (scale bar: 5 mm). 70

Figure 5.2 Optical microscope images of sucrose templates pulled at (a) 25.6 and (b) 2.0 cm/s in side and cross-section views. Scale bars: 100  $\mu\text{m}$ . (c) The template diameter as a function of the pulling speed. The dotted curve represents an 72

exponential decay. (d) An AFM scan image over a  $4 \times 4 \mu\text{m}^2$  area on a sucrose template.

Figure 5.3 An end-to-side junction formed between two sucrose templates in (a) a side and (b) bird's eye view. (c) Steam-bonding is also effective between templates with greatly dissimilar diameters. (d) A MF channel branch PDMS-replicated from (c). The junction is located on the far side but is clearly visible, confirming the transparency of the MF channel. (e) A 3D assembly of three internally looped templates to a cylindrically tapered backbone. No loop is in the same plane with another. (f) A 3D MF network made with (e). Scale bars: (a)-(d)  $600 \mu\text{m}$ , (e)-(f)  $5 \text{ mm}$ .

Figure 5.4 Vaso-mimetic MF architectures: (a) A tapered junction between two sucrose templates bonded with water-based adhesive. (b) A PDMS MF channel molded from (a) with red dye flowing through the branch. (c) A stenosis-like structure formed by localized thermal deformation of the sucrose template (inset) and its PDMS molding. Scale bars:  $300 \mu\text{m}$ .

**LIST OF TABLES**

Table 2.1  $L_{prop,2D}$  (in cm) obtained from 2D numerical mode analyses using different combinations of the structural parameters  $d_s$ ,  $w$ , and  $h$  values (all in  $\mu\text{m}$ ). Due largely to the ripples in the  $L_{prop,2D}$  spectral curves shown in Figs. 2.3 and 2.5, the values exhibit substantial changes corresponding to variations in the structural parameters in the length scale of 100 nm. The best result was obtained when  $d_s = 2.9 \mu\text{m}$ ,  $w = 9.1 \mu\text{m}$ , and  $h = 3.3 \mu\text{m}$ . 31

## ACKNOWLEDGEMENTS

First of all, I would like to express my sincere gratitude to my major professor, Dr. Jaeyoun Kim. Since I have entered the graduate school in fall 2007, Dr. Kim has given me so much guidance and has helped make this degree possible. Also, Dr. Kim has inspired me with his passion for research and his active engagement with his students. I will continue to be impacted by the life lessons he has shown me by always finding joy in researching new areas and collaborating with other colleagues. Not only has Dr. Kim exhibited excellence as an advisor, but he has also shared so much of his technical knowledge pertaining to the experiment, which further enriched my graduate study.

I also would like to thank my program of study committee members. I am indebted to Dr. Robert Weber, as it was a privilege taking his classes, completing the independent study, and working as a teaching assistant under him. It was a complete blessing to observe his passion and brilliance in the laboratory. I cannot thank Dr. Mani Mina enough for his shared wisdom and guidance throughout my undergraduate and graduate experience. He has taught me countless things about learning, teaching, and collaborating with others. I also want to show my gratitude to Dr. Liang Dong and Dr. Santosh Pandey for serving as my committee members and sharing their insights on the research and experiments. Finally, I am very grateful to Dr. Kai Ming Ho, for his support as the former POS member.

I also would like to thank my parents, friends, and loved ones for their support and encouragement. Without their unconditional love and affirmation, especially from my mother and father, I would not have made it to this point.

Last and foremost, I thank my Father in heaven who has given me this life and led me during this journey. All I am is His.

## ABSTRACT

Bioengineering is an emerging field of study which bridges life science and engineering. At its early stage, bioengineering was commonly recognized as biomedical engineering. This focused mainly on the biomedical aspects with the engineering playing only assistive roles. Pharmaceutical researches, such as cell mechanics, vascular biology, and neural engineering, have been performed as its sub-categories. Later, with increased emphasis on the engineering aspect, a new phase of bioengineering has emerged. Biomimetics, the effort to mimic nature and utilize biological inspirations, is this new branch.

The advances in microfabrication techniques during the last few decades have further promoted bioengineering. Micro/electromechanical systems (MEMS) technologies to obtain microscale total assay systems ( $\mu$ TAS) have led to microfluidics studies that are directly related to biomedical studies. Soft lithography and polymer MEMS have facilitated the development of biomimetics.

Despite rapid advancement in the field of bioengineering, many areas of development remain. This especially pertains to miniaturization, cost deduction, and ease of fabrication in polymer MEMS technologies, which are crucial in both biomedical and biomimetic aspects. However, the broad and inclusive nature of bioengineering makes it difficult to choose a particular subject to focus on. Therefore, we extracted key factors in bioengineering: microfluidics, bio-inspired structures, polymer MEMS, and their sensor applications. In accordance, I will present four platform technologies which are correlated to all key factors synergistically.

First, the optofluidic waveguiding was studied to enhance sensing capability in biomedical studies. Utilization of optical components in sensing scheme has been attracting

interests for its electromagnetic interference (EMI)-free nature. However, one of the biggest difficulties in optofluidic sensing is that the liquid core generally exhibits refractive index lower than the solid claddings, making total internal reflection impossible. A design which adopts anti-resonance reflection optical waveguiding (ARROW) scheme was designed and analyzed with 2D numerical simulations.

Secondly, polymer MEMS technology was investigated to make bio-inspired optical waveguiding structures. There have been growing demands for polymer microwires due to their actuator and sensor potentials. By utilizing poly(dimethylsiloxane) and sacrificial water-soluble wax in combination, we could generate two dimensional arrays of microscale polymer waveguides that are strongly attached to the super/substrate. Mechanical and optical characterizations were performed to show its potentials.

Thirdly, a gas flow sensor was developed based on the previously developed polymer microwire. Due to its flexibility, the microwire can be elongated up to a few times its original length in addition to its tension and resistance to the outside mass flow increased. By investigating their relationship, we have shown the potential of the microwire to be used as a tunable optical gas flow sensor.

Finally, we developed a new and easy method to mimic biological blood vessels with microfluidic channels completed with circular cross-sections and three dimensional (3D) topologies. We have found the biomaterial which makes the fabrication simple, safe, cost-effective, and environment-friendly. As an example, we produced complex 3D assemblies of channels with their diameters ranging between 30 to 400  $\mu\text{m}$ .

When integrated synergistically, these unit structures and functionalities, mainly based on optical and/or polymer technologies, will greatly facilitate the realization of future bioengineering application systems.



## CHAPTER 1. Introduction

### 1.1 Research motivations

Bioengineering, as the words ‘bio’ and ‘engineering’ imply, is a study which correlates life science and engineering disciplines [1]. This application-oriented field was created so that problems of one area can be promptly paired with techniques from the other area [2]. During the last few decades, the attention toward bioengineering has been further increased along with the advancements in microfabrication technologies, which have enabled small scale lab-on-a-chip fabrications [3]. Thanks to its multidisciplinary nature, bioengineering offers limitless prospects in many fields of study [4]. Presently, the gap between engineering and science in this discipline causes blurred vision [1,5]. Therefore, we have to survey the fields from both scientific and engineering points of view.

#### 1.1.1 Biomedical engineering

In one point of view, bioengineering focuses on biomedical and life science with engineering and technology just functioning as tools [6]. Biomedical engineering and biotechnology [1,6] are additionally established terms which validate their emphasis on the substance of biomedicine. Some major sub-disciplines of biomedical engineering are cell mechanics [2,7,8], vascular engineering [9,10], and neural engineering [1,11] if they are categorized by their targets of study.

Cell mechanics is the study of mechanical properties of cells to enhance drug deliveries and disease treatments. Chen *et al.* investigated how the stiffness of metastatic cells differs from that of healthy cells [7]. To study cells, researchers have focused on developing effective and non-invasive ways of cell sorting [12], cell trapping [2], and cell analyzing

devices [2,8]. Vascular engineering deals with techniques used to study blood vessel structures and their mechanics to solve problems related to their abnormality or diseases. As Bellan *et al.* presented in their paper, it is important to generate artificial vessel-like capillaries (less than  $10\mu\text{m}$ -size vessels) and investigate the effect of stresses and flow-motion inside the channel [10]. Neural engineering focuses on technological development to aid the study of nerve systems which, in turn, will enhance medical and surgical treatments [6]. Figure 1.1 (a,b) shows examples of cell mechanics and vascular study.

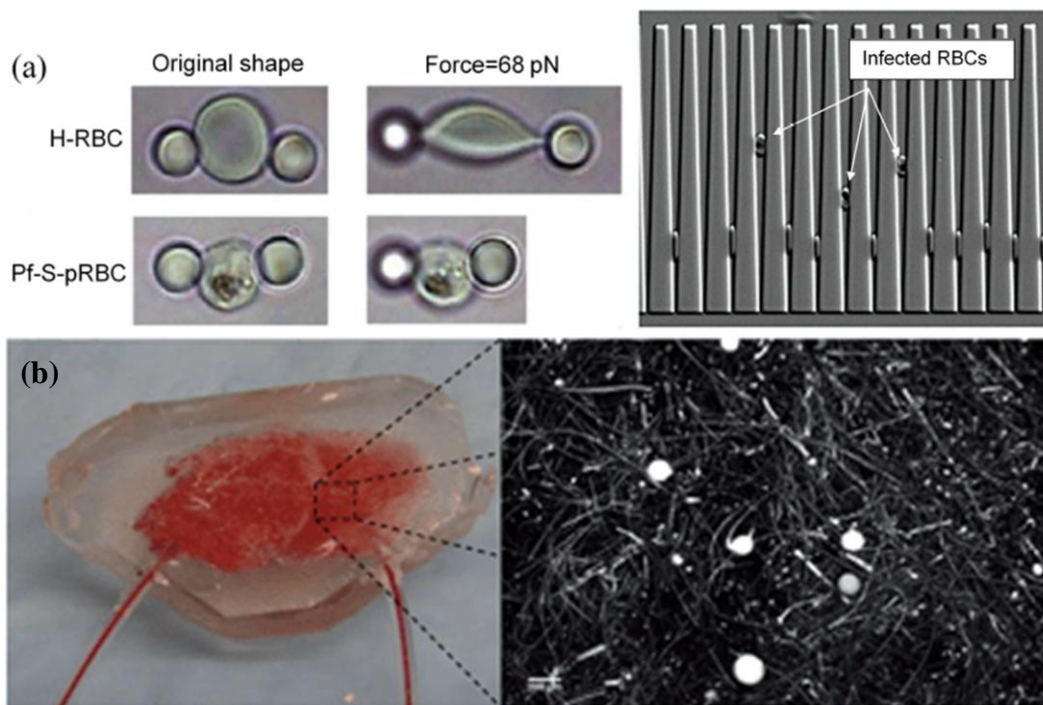


Figure 1.1 (a) Healthy and infected red blood cells (RBCs) show different levels of stiffness and trapping probability in the capillaries (from ref [8]), (b) Vasomimetic structure and its microscopic view (from ref [9]) to give biomedical technology examples.

From descriptions of sub-disciplinary studies, we can recognize the fact that the majority of those areas deals with certain forms of fluidic systems like vessels in the living organisms. Thus, we need to focus on the research and development of microfluidics (MF), the study of fluidics in micron scale as well as the development of fabrication techniques [3].

### 1.1.2 Biomimetics

In another aspect of bioengineering, the improvements of engineering discipline are predominantly concerned while the biological studies of nature are employed as the inspirations [5]. Biomimetics, termed by Otto Schmitt in 1969, is made out of ‘bios’ and ‘mimesis’ to describe imitation of life [5]. Scientists and engineers have been fascinated by nature for its optimal way from evolutionary development [13]. However, the complicated and compact structures in nature made their mimicry unfeasible. Another challenge involved substituting the soft structures of nature with the hard materials that dominated early microfabrication technologies.

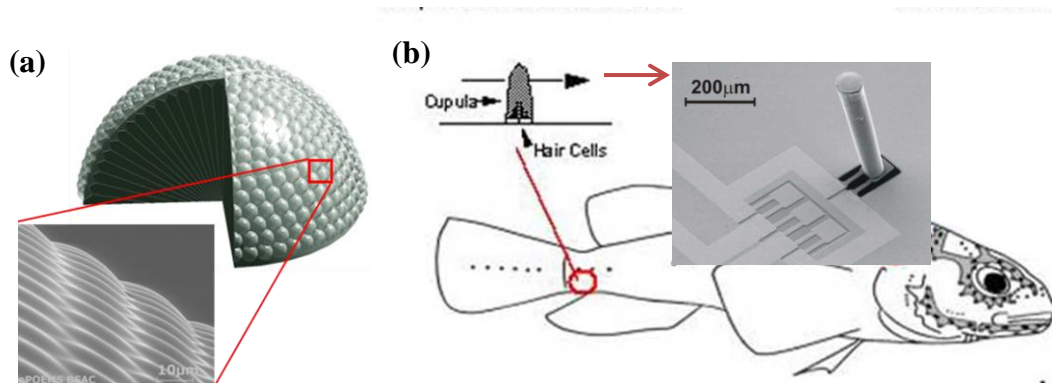


Figure 1.2 (a) Artificial compound eyes (from ref [14]) and (b) an artificial hair cell (from ref [15]) to show well-known biomimetic examples.

With the advances in microfabrication technology, biomimetics have developed into several areas: biomaterials, biomimetic structures, and biomimetic sensors. Figure 1.2 shows two different biomimetic structures. For instance, chemical engineers studied the silk worms and developed polymer materials [16]. Engineers with mechanical backgrounds studied the flying insects and developed artificial flying robots by analyzing and mimicking the flying scheme [17,18]. Other researchers from nanotechnology developed adhesive nano-structures by mimicking the Gecko's foot [19].

<p><b>Acoustic</b></p> <ul style="list-style-type: none"> <li>Cochlear amplifier</li> <li>Cochlear speech recognition system</li> <li>Dolphin based sonar receiver</li> <li>Binaural dolphin echolocation system</li> <li>Micro echolocation system</li> <li>Binaural bat echolocation system</li> </ul> <p><b>Chemical</b></p> <ul style="list-style-type: none"> <li>Artificial human tongue</li> <li>Artificial chemical recognition sites</li> <li>Piezoelectric artificial human nose</li> <li>Conducting polymer artificial human nose</li> <li>Chemo-fluorescent artificial human nose</li> </ul> <p><b>Electric</b></p> <ul style="list-style-type: none"> <li>Artificial electrolocation device</li> <li>Fly based vision system</li> <li>Fly based, hexagonal oriented vision system</li> <li>Fly based, non-camera motion detection system</li> <li>Artificial bilayer lipid membrane</li> <li>Primate eye based vision system</li> <li>Human eye based vision system</li> <li>Artificial muscle monitoring</li> </ul>	<p><b>Optical</b></p> <ul style="list-style-type: none"> <li>Artificial ommatidia array</li> <li>Vision-based magnetic compass</li> </ul> <p><b>Mechanical</b></p> <ul style="list-style-type: none"> <li>Artificial halters</li> <li>Artificial muscle spindle</li> <li>Artificial meissner corpuscles</li> <li>Artificial lateral line system</li> <li>Artificial arthropod hair cell</li> <li>Artificial cricket filiform hair array</li> <li>Campaniform sensillum strain sensor</li> <li>Carbon microcoil tactile sensors</li> <li>Electroactive polymer muscle</li> <li>Micromachined campaniform sensillum strain sensor</li> <li>Artificial posture monitoring</li> <li>Artificial crustacean antenna</li> </ul> <p><b>Thermal</b></p> <ul style="list-style-type: none"> <li>Photo-mechanical IR Sensor</li> <li>ThermalSkin</li> </ul>
---	--

Figure 1.3 Summary of biomimetic sensors (from ref [4]) which states its popularities and on-going researches in different disciplines.

Bio-inspired sensors, among others, have gained the most attention because high-tech devices demand integrated sensors to monitor and respond to changes in their environments.

This enables us to find various, brilliant and highly sensitive mechanisms in nature [15]. Fan et al. demonstrated this in their flow sensor in which they studied and imitated the way fish sense the water flow by studying lateral lines [20]. Figure 1.3 from Stroble *et al.*'s 2009 paper [4], enumerates various biomimetic sensors investigated.

Of course there also are cases where bio-inspired structures are used for biomedical applications and result in equally strong advances on both areas. One such example is the vasomimetic channel which targets directly to mimic the nature's biological structure and is further used in the advancement of biomedicine [9].

## 1.2 Overview of current technologies

### 1.2.1 Microfluidics and Microfabrication

Microfluidics (MF) was initially defined as a study dealing with the process and control of micron-scale fluid. As various life science and engineering disciplines have utilized MF, the field of MF has extended to the fabrication technologies and the microsystem integrations of micro/nano scale fluidics [3].

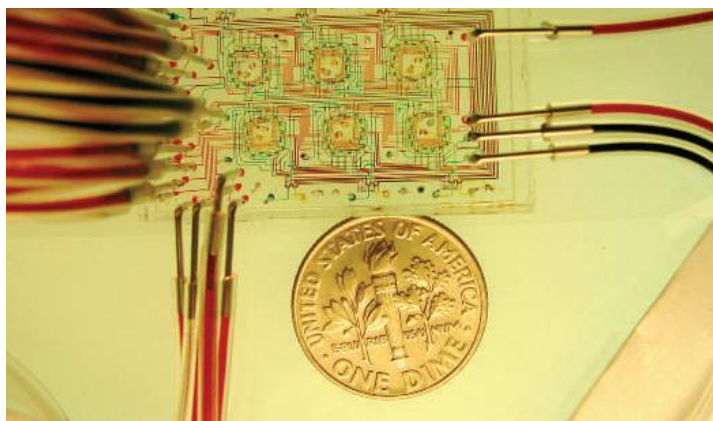


Figure 1.4 Chip-based 16 nanoliter bioreactors for bacteria (from ref [20]) which illustrate one of the microfluidic applications.

Bioengineering, as previously mentioned, has a close relation with the improvement of MF. In particular, the realization of micro total assay system ( $\mu$ TAS) for pharmaceutical studies, such as screening cells, has been greatly facilitated by MF during the last few decades [6]. Figure 1.4 shows one  $\mu$ TAS structure from F. Balagadde *et al.*'s paper [20].

Microfabrication techniques for micro/electro-mechanical systems (MEMS) have also been greatly advanced in conjunction with the growth of microfluidics throughout the last few decades [3]. Various MEMS techniques, such as deposition, etching, and bonding for selective areas, have been adopted to fabricate MF channels [3]. Several silicon based MEMS techniques have especially proven their capability of making nano-channels as shown in Pimpin *et al.*'s review paper [22]. However, technologies are more focused on hard (silicon-based) MEMS in addition to planar and rectangular cross-sectional structures [23]. To attain the true bio-inspired MF structures, we need soft channels with the circular cross-section and preferably three dimensional topologies [23].

### 1.2.2 Soft lithography and Polymer MEMS

Soft lithography is a microfabrication method which utilizes the elastomer molding to realize the microfluidic channels and related structures [24]. Thermally curable polymer, poly-dimethylsiloxane (PDMS), is commonly used as an elastomer for its ease of handling, transparency and flexibility. Figure 1.5, from Whitesides *et al.*' 1998 paper [24], illustrates some of soft lithography methods such as replica molding (RM), microtransfer molding ( $\mu$ TM), and micromolding in capillaries (MIMIC). Soft lithography has enabled easy patterning of nanometer scale structures which provide solutions in bioengineering [25].

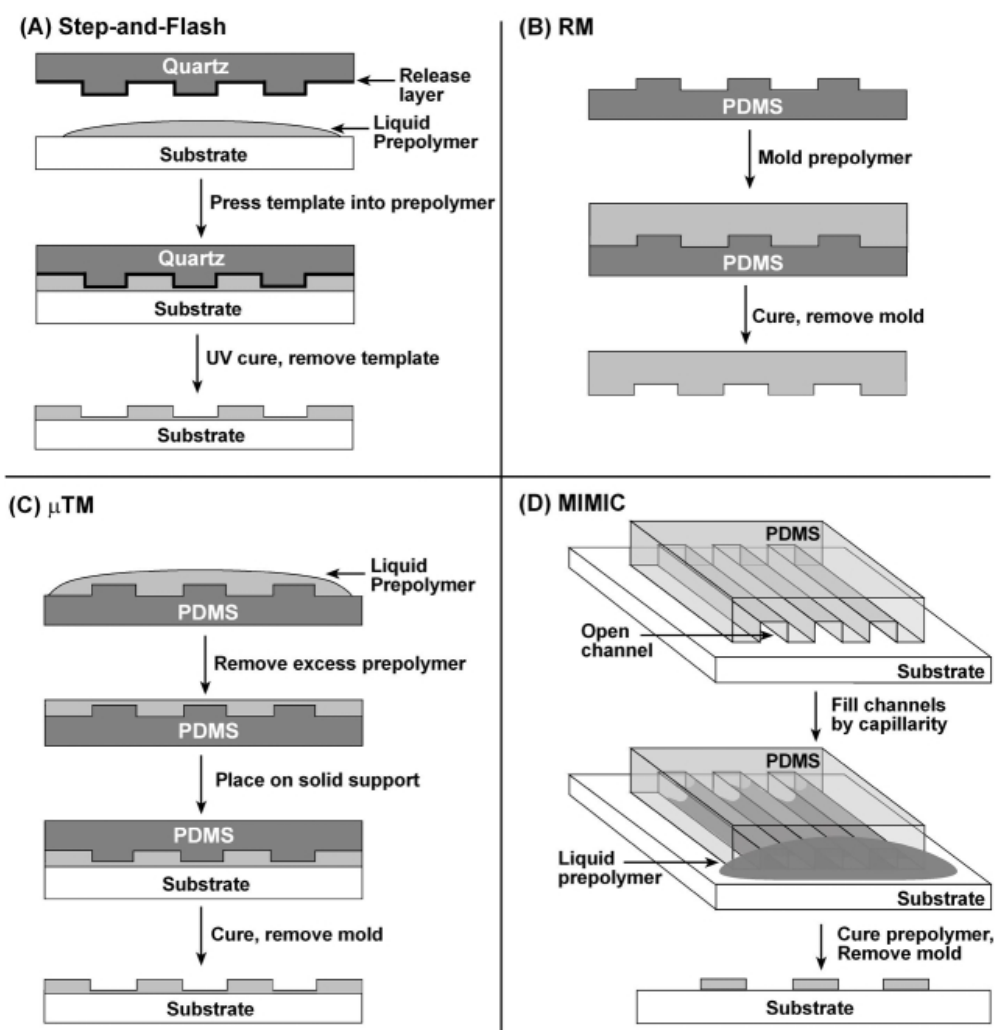


Figure 1.5 Four kinds of Soft lithography depending on the fabrication methods (a) step and flash (b) replica molding (c) microtransfer molding (d) micromolding in capillaries (from ref [24].)

The advent of polymer-based MEMS technologies has expedited the development of biotechnology. Soft MEMS is another name to describe the usage of plastic/elastomer materials in MEMS as film substrates or membranes and other structures [25]. Polymer MEMS structures provide the advantages of flexibility, strain resistance, and low cost over hard Si-MEMS, which make them great candidates for biomedical applications. Also,

polymer MEMS can be employed to imitate biological structures such as fiber bundles [14] in amphipod eyes or as hair cells [15] in fish to develop microscale sensor structures.

In this overview, we have outlined the necessity for MF and soft MEMS-based platform technologies in biomedical and biomimetic applications. Next, we specify the challenges and approaches associated with them.

### **1.3 Challenges**

#### **1.3.1 Miniaturization**

Since the emergence of MEMS technologies, achieving accurate lab-on-a-chip devices with sensors and total assay systems all integrated in a single chip has been intensely sought after [2]. Chen *et al.* introduced a lab-on-a-chip capillary network to capture and test a single red blood cell ( $3\mu\text{m} \times 5\mu\text{m}$ ) with some channels as small as  $8\mu\text{m} \times 5\mu\text{m}$  [7]. Moreover, to imitate nature's compact and complex design, such as the compound eyes of insects for the wide-field-of-view [14], biomimetic structures also require submicron scale fabrication technologies.

Currently, some of hard (silicon-based) MEMS fabrication techniques, such as electron beam lithography [22], seem to promise solutions for the miniaturization down to 5nm. However, as previously discussed, we need structures based on soft (polymer-based) MEMS technologies, which are the most feasible at obtaining several microns or larger in scale [26] or else existing only in simple forms [23].



### 1.3.2 Cost deduction

Even if some existing research works have potential to achieve the miniaturization, they are often too expensive due to their use of expensive equipment, clean room facilities, and the process materials. Moreover, the formerly available commercial analysis assay for biomedical study was unnecessarily big and bulky which added material/process expenses [27]. As a result, the development of low-cost process became essential.

Soft MEMS technologies have attempted to resolve this high-cost problem by potentially removing silicon substrate and expensive equipment [25]. For instance, MF channels made with PDMS molding process require a spinner, a UV light, hot plates, and a few polymers whereas hard MEMS technologies require higher cost processes, such as with chemical vapor deposition (CVD) or deep reactive ion etching (DRIE) [3]. However, the soft MEMS technologies are still in the earlier stage of development and there is more room to explore.

### 1.3.3 Easy fabrication

Ease of fabrication is also important. Biomimetic efforts focus on simple yet elegant approaches as observed in nature. Soft MEMS is one good candidate, but current technologies are limited to planar/simple trajectory structures. Smarter designs and technologies are on demand as well as their easy fabrication methods.

We also have to pay attention to the optical components that can be easily fabricated and integrated in polymer MEMS devices to provide smarter functionalities. Optical schemes are also free from electromagnetic interference (EMI) which makes them increasingly popular in biomedical sensing and imaging applications. However, there have been only a few polymer-based optical devices, which is a small number in comparison with those available in nature.

## 1.4 Approaches

So far, we have discussed the increasing interests and needs for bioengineering, suitability of soft MEMS technologies for biomedical and biomimetic systems, and existing challenges for additional developments. From the discussion, we can extract target subjects to be further explored: bio-inspired structures, microfluidics, polymer MEMS, and optical sensing applications. Since we are new to these areas, developing platform technologies, the underlying technologies for future development, would be beneficial. In particular, simple fabrication processes that can easily be repeated without expensive facilities are preferred. Four platform technologies are to be established:

1) Optofluidics: Microscale fluidic devices which utilize optical functionalities should be studied to enhance biomedical and environmental sensing schemes. One of the major obstacles to utilize optical sensing in the fluid is in waveguiding along the liquid core which has generally lower refractive index than the solid cladding. An alternative waveguiding scheme of total internal reflection (TIR) will be investigated with the simulation tools.

2) Polymer MEMS: Fabrication techniques for elastomer-based microscale optical fibers, which mimic a bundle of optical waveguides, are to be investigated. Microscale polymer fibers have potential to be utilized in biomimetic imaging devices as well as tunable mass-flow sensors.

3) Bio-inspired sensor: Studies to develop a mass flow sensor is to be performed based on soft MEMS process and microfluidic integration. The development process benefited from both bio-inspired operation principles and experimental studies linking the tension of the polymer and throughput power.

4) Vasomimetic device development: Generating MF channels, which mimic the blood vessel networks in the human body, requires both microfluidic and biomimetic aspects fulfilled with soft MEMS techniques. We especially focus on physiological realism with circular cross-sections and three dimensional trajectories.

### 1.5 Thesis Organization

The following chapters are an accumulation of the four published journal papers of which I am the first/primary author.

Chapter 2 illustrates the optofluidic waveguide which suggests an effective way of guiding the light in the liquid core with a low-refractive index surrounded by the solid claddings with a higher index. Waveguiding is significant for optical sensing in microfluidic channels that the paper introduces the design based on anti-resonance reflection optical waveguiding. It is modified from the journal paper, “Two-dimensional optofluidic liquid-core waveguiding based on optimized integration of single- and multiple-layer ARROWs,” published in *Journal of the Optical Society of America B*, vol 28, 2011.

Chapter 3 introduces the biomimetic optical waveguides which are inspired from the deep-sea amphipod eyes. Soft lithography and water-soluble wax-based fabrication methods will be presented in detail. The surface investigation and mechanical and optical properties are also illustrated. The paper, “Fabrication of strongly anchored, ultrahigh aspect-ratio elastomeric microwires for mechanical and optical applications,” is published in the *Journal of Micromechanics and Microengineering*, vol 21, 2011.

Chapter 4 demonstrates the utilization of a microwire structure developed in chapter 3 as a gas flow sensor. By applying lateral tension, the optical throughput has been changed

which enables tunable mass flow sensing. The chapter is modified from “Elastomeric microwire-based optical gas flowmeter with stretching-enabled tunability in measurement range,” published in *Optics Letter*, vol 33, 2011.

Chapter 5 illustrates a new bio-inspired solution to make Vasomimetic structures. By utilizing the sucrose as a sacrificial material, we could easily make real vessel-like circular cross-sectional fluidic channels in the range of 30 to 500  $\mu\text{m}$  with three dimensional topologies. The chapter is modified from the journal paper, “Sucrose-based fabrication of 3D-networked, cylindrical microfluidic channel for rapid-prototyping of lab-on-a-chip and vaso-mimetic device,” currently published in *Lab on a Chip*, 2012.

Finally, the conclusion and future aspects will be summarized in Chapter 6.

## 1.6 References

- [1] Z. O. ABU-FARAJ, “Bioengineering/Biomedical Engineering Education and Career Development: Literature Review, Definitions, and Constructive Recommendations,” *Int. J. Engng Ed.*, **24**, p.990 (2008)
- [2] C. Moraes, C. A. Simmons, and Y. Sun, “Cell Mechanics Meets MEMS,” *CSME Bulletin*, N/A, (2006)
- [3] J. D. Zahn (editor), “*Methods in bioengineering: Biomicrofabrication and biomicrofluidics*,” *Artech House*, Lonson (2010)
- [4] J.K. Stroble, R.B. Stone, and S.E. Watkins, "An overview of biomimetic sensor technology", *Sensor Review*, **29**, p.112 (2009)

- [5] J. F. V. Vincent, “Biomimetics – a review,” *Proc. IMechE*, **223**, p.919 (2009)
- [6] M.R. El-Gewely, “Biotechnology domain,” *Elsevier*, **1**, p.5 (1995)
- [7] Y.-C. Chen, G.-Y. Chen Y.-C. and Lin G.-J. Wang, “A lab-on-a-chip capillary network for red blood cell hydrodynamics,” *Microfluid Nanofluid*, **9**, p.585 (2010)
- [8] C. T. Lim and A. Li, “Mechanopathology of red blood cell diseases — Why mechanics matters,” *Theor. Appl. Mech. Lett.*, **1**, p.014000-1, (2011)
- [9] L. M. Bellan, S. P. Singh, and P. W. Henderson, T. J. Porri, H. G. Craigheada and J. A. Spector, “Fabrication of an artificial 3-dimensional vascular network using sacrificial sugar structures,” *Soft Matter*, **5**, p.1354 (2009)
- [10] A. D. van der meer, A.A. Poot, M. H. G. Duits, J. Feijen, and I. Vermes, “Microfluidic Technology in Vascular Research,” *J. of Biomed. and Biotech.*, **2009**, p.1, (2009)
- [11] J. Li, S. Connell, and R. Shi, “Biomimetic Architectures for Tissue Engineering,” *Intech Ch24*, p.487 (2010)
- [12] A. Asgar, S. Bhagat, H. Bow, H. W. Hou, S. J. Tan, J. Han , C. T. Lim, “Microfluidics for cell separation,” *Med Biol Eng Comput*, **48**, p.999, (2010)
- [13] Y. Bar-Cohen, “Biomimetics: Using nature as an inspiring model for human innovation,” *Bioinspir. Biomim.*, **1**, p1 (2006)
- [14] J. Kim, et al, “Artificial ommatidia by self-aligned microlenses and waveguides,” *Opt. Lett.*, **30**, p.5 (2005)

- [15] M. E. McConney, K. D. Anderson, L. L. Brott, R. R. Naik, and V. V. Tsukruk, "Bioinspired Material Approaches to Sensing," *Adv. Funct. Mater.*, **19**, p.2527, (2009)
- [16] J. G. Hardy and T. R. Scheibel, "Silk-inspired polymers and proteins," *Biochem. Soc. Trans.*, **37**, p.677, (2009)
- [17] F. Li, W. Liu, C. Stefanini, X. Fu and P. Dario, "A Novel Bioinspired PVDF Micro/Nano Hair Receptor for a Robot Sensing System," *Sensors*, **10**, p.994 (2010)
- [18] R. Armour, K. Paskins, A. Bowyer, J. Vincent and W. Megill, "Jumping robots: a biomimetic solution to locomotion across rough terrain", *Bioinspir. Biomim.* **2**, S65 (2007)
- [19] A.K. Geim, S.V. Dubonos, I.V. Grigorieva, K.S. Novoselov, A. A. Zhukov, and S. Y. Shapoval, "Microfabricated adhesive mimicking gecko foot hair," *Nature Materials*, **2**, p. 461 (2003)
- [20] Fan, Z., Chen, J., Zou, J., Bullen, D., Liu, C. and Delcomyn, F., "Design and fabrication of artificial lateral line flow sensors", *J. of Micromech and Microeng.*, **12**, p. 655 (2002)
- [21] F. K Balagadde, L. C. You, C. L. Hansen, F. H. Arnold, S. R. Quake, "Long-term monitoring of bacteria undergoing programmed population control in a microchemostat." *Science* **309**, p.137 (2005)
- [22] A. PIMPIN, W. SRITURAVANICH, "Review on Micro- and Nanolithography Techniques and Their Applications." *Engineering Journal*, Thailand, 16, Nov. 2011.

- [23] J. Lee, J. Paek, and J. Kim, "Sucrose-based fabrication of 3D-networked, cylindrical microfluidic channel for rapid-prototyping of lab-on-a-chip and vaso-mimetic device," *Lab Chip*, (2012)
- [24] Y. Xia and G. M. Whitesides, "Soft lithography," *Annu. Rev. Mater. Sci.*, **28**, p.153 (1998)
- [25] Chang Liu, "Recent Developments in Polymer MEMS," *Adv. Mat.* **19**, p.3783 (2007)
- [26] J. Lee and J. Kim, "Elastomeric microwire-based optical gas flowmeter with stretching-enabled tunability in measurement range," *Optics Letters*, **36**, p.3789 (2011)
- [27] B. Prabhakarandian, M.-C. Shen, K. Pant, M. F. Kiani, "Microfluidic devices for modeling cell-cell and particle-cell interactions in the microvasculature," *Microvas. Res.*, **82**, p.210 (2011)

## **CHAPTER 2. Two-dimensional optofluidic liquid-core waveguiding based on optimized integration of single- and multiple-layer ARROWs**

Modified from a paper published in *Journal of the Optical Society of America B*

Jiwon Lee,<sup>1</sup> Zhuo Ye,<sup>2</sup> Kai-Ming Ho,<sup>2</sup> and Jaeyoun Kim<sup>1,\*</sup>

### **2.1 Abstract**

We present a novel 2D liquid-core waveguiding scheme which combines two different types of ARROWs to achieve ease of fabrication and richer optofluidic functionalities. We established the conditions for the optimal integration of the two ARROW schemes theoretically and validated them with 2D numerical mode analysis. The proposed scheme also provides a convenient means to install supporting solid-core waveguides without additional burden in fabrication.

### **2.2 Introduction**

Schemes to confine optical waves within a volume of material with refractive index lower than that of its ambience have been the object of intense research [1]. The unavailability of total internal reflection (TIR) in such an inverted core-cladding index distribution has led to the employment of many other mechanisms, with the anti-resonance reflection optical waveguiding (ARROW) as the most prominent choice. With the emergence of microfluidics, there have been incessant efforts to realize liquid-core waveguides (LCWs) by guiding light along the body of liquid confined within the microfluidic channels [1,2]. Since typical liquid materials exhibit refractive indices lower than those of solid microfluidic



channel materials, the ARROW scheme has seen an increasing level of adoption in LCWs as well.

The ARROW configuration for LCW, however, differs significantly from that for solid-core waveguiding in one important aspect. In the latter case, originally devised to confine light within a low-index solid stripe placed on a high index substrate, the ARROW layers are deposited only along the bottom side of the stripe, leaving the remaining three sides exposed to the surrounding materials with even lower indices, usually air, to induce TIR [3]. The liquid-core, however, needs to be confined within a microfluidic channel and the ARROW layers must be deposited along all four sides, both horizontally and vertically, of the channel. This additional requirement can complicate the achievement of the LCW significantly.

Previously, ARROWs fully surrounding a microfluidic channel have been realized by depositing ARROW layers over a trench-structure and closing it with a superstrate deposited with another set of ARROW layers [4]. Another method is by depositing the ARROW layers over a sacrificial core placed on an ARROW substrate and dissolving the core subsequently [5]. In either case, the ARROW layers for vertical walls need to be deposited simultaneously with the ones for horizontal walls and the difference in their deposition rates could make the thickness control difficult and inaccurate. The use of sacrificial cores or deep-etched trenches further complicates the fabrication.

In this work, we propose a new LCW configuration which utilizes a combination of two different ARROW schemes to achieve a simpler fabrication and richer optofluidic functionality. Figure 2.1 shows the proposed LCW scheme along with major structural and material parameters. While a pair of conventional multiple-layer (ML) ARROWs was used to confine light in the vertical direction, only a pair of dielectric ridges was installed for the

lateral light confinement. Since each ridge functions as an ARROW using only a single layer, it will be referred to as the single-layer (SL) ARROW.

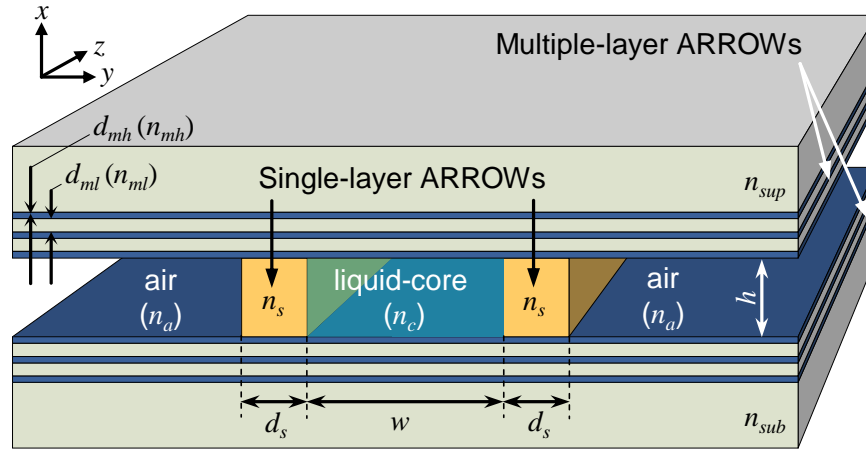


Figure 2.1 The proposed liquid-core waveguide that integrates the single layer (SL)- and multiple layer (ML)-ARROWs. The SL-ARROWs also function as the microfluidic channel walls and the spacer which separates the two ML-ARROWs.

Integrating the SL- and ML-ARROWs brings in many advantages. First, it allows separate realizations of the optical confinement mechanisms in vertical and lateral directions, i.e., ML-ARROWs by thin film deposition on flat slabs and SL-ARROWs by photo- or soft-lithographic patterning on one of the slabs. Then the top ML-ARROW can be installed using the SL-ARROWs as the spacer. Secondly, the SL-ARROW ridges can be wide enough to function as the walls of microfluidic channels. This eliminates the structural difference between the microfluidic channels with or without the LCW capability, allowing their simultaneous fabrication with a single patterning step. The SL-ARROW ridges can also function as solid-core waveguides running in contact with a LCW, which is ideal for mode coupling and light delivery.

The concept of using a pair of single dielectric layers to confine light within a lower index material in between was proposed by Goltser *et al.* for semiconductor lasers [6]. Litchinitser *et al.* also showed that, in ARROWs made of optically thick dielectric layers, the first cladding layer plays the main role in the confinement [7]. However, its integration with another waveguiding mechanism for microfluidic LCW has been rare. In Ref. [8], Lunt *et al.* demonstrated a single over-coating ARROW in which the ML-ARROW surrounding the top, left, and right sides of the sacrificial core in Ref. [5] was replaced by a single dielectric layer. Even though the modification simplified the fabrication and light coupling, it left the difficulty in simultaneously depositing the vertical and horizontal layers unaddressed. Note that, despite the visual similarity, our scheme is different from those of Refs. [9] and [10] which employ ML-ARROWs for both vertical and horizontal confinements. Our scheme further differs from the one in Ref. [11] which considers only the ray propagation between the TIRs in the solid claddings around the liquid-core, but not the interference between the rays or 2D confinement.

### 2.3 Theoretical Backgrounds

For LCW applications, the  $e^{-1}$  propagation distance  $L_{prop}$  is the most important parameter that must be maximized by optimizing the two ARROWs individually as well as collectively. To that end, we will first obtain the lateral confinement condition in 1D and then extend the result to optimize the 2D LCW.

Figure 2.2 shows the ray model of the 1D LCW derived from Fig. 2.1 by assuming the liquid-core, SL-ARROW, and air layers are infinite in the  $x$ -direction. Regarding the SL-

ARROW itself, it is well-known from the ARROW principle [3] that the anti-resonance reflection maximizes when the phase difference at the phase-front  $c-c'$

$$\Delta\varphi_l \equiv 2k_o n_s d_s \cos \theta_2 + \varphi_{TIR} = 2m\pi \quad (1)$$

where  $m$  is an integer,  $k_o = 2\pi/\lambda_o$ ,  $\varphi_{TIR} = \pi - 2 \cdot \text{atan} [(\sin^2 \theta_2 - (n_a/n_s)^2)^{1/2}/(P \cdot \cos \theta_2)]$ , and  $P = 1$  or  $(n_a/n_s)^2$  for TE or TM, respectively [12]. Conversely, the anti-resonance reflection vanishes when

$$\Delta\varphi_l = (2m+1)\pi. \quad (2)$$

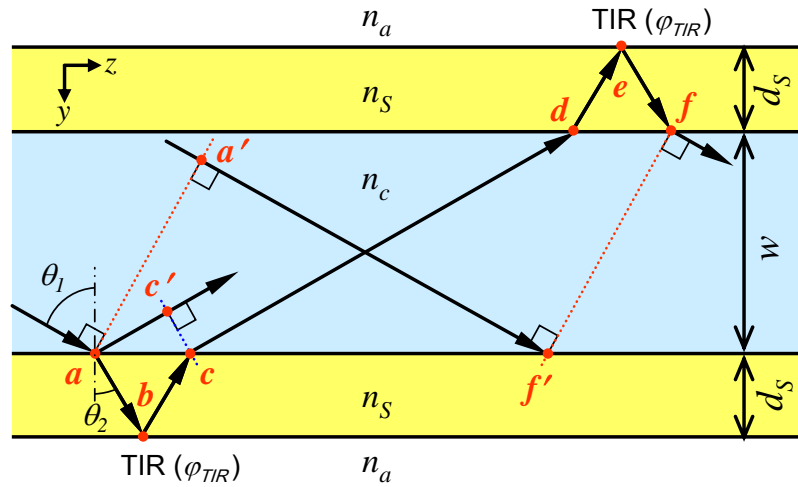


Figure 2.2 The ray model for the lateral confinement configuration based on the SL-ARROW/Liquid-Core/SL-ARROW structure.  $n_s > n_c > n_a$  is assumed.

Secondly, to confine light efficiently within the liquid-core between two SL-ARROWs, it is also necessary to enforce constructive interference between the rays which traveled the two

separate paths  $a \rightarrow f$  and  $a' \rightarrow f'$  at the  $f-f'$  phase-front. Based on simple geometry, it is straight forward that:

$$\varphi_{a' \rightarrow f'} = k_o n_c [4 \cdot d_s \tan \theta_2 + w \cdot (\tan \theta_1 - \cot \theta_1)] \cdot \sin \theta_1, \quad (3)$$

$$\varphi_{a \rightarrow f} = 4 k_o n_s d_s \sec \theta_2 + k_o n_c w \sec \theta_1 + 2 \cdot \varphi_{TIR}. \quad (4)$$

Therefore, the condition for efficient LCW is:

$$\Delta\varphi_2 \equiv \varphi_{a' \rightarrow f'} - \varphi_{a \rightarrow f} = 2q\pi \quad (5)$$

where  $q$  is an integer. Using Snell's law  $n_c \sin \theta_1 = n_s \sin \theta_2$ , the difference between the first terms of Eqs. 3 and 4 can be simplified as:

$$4 k_o n_s d_s \sec \theta_2 - 4 k_o n_c d_s \tan \theta_2 \sin \theta_1 = 4 k_o n_s d_s \cos \theta_2, \quad (6)$$

which enables us to rewrite Eq. (5) as:

$$\Delta\varphi_2 = 4 k_o n_s d_s \cos \theta_2 + 2\varphi_{TIR} + k_o n_c w \cdot (\sec \theta_1 - \tan \theta_1 + \cot \theta_1) = 2q\pi. \quad (7)$$

Note that the first two terms of Eq. (7) equal  $2 \cdot \Delta\varphi_1$  which has already been enforced to be an integer multiple of  $2\pi$  in Eq. (1). Therefore, the final form of the waveguiding condition is:

$$\sec \theta_l - \tan \theta_l + \cot \theta_l = q \cdot \lambda_o / (n_c \cdot w), \quad (8)$$

The conditions imposed by Eqs. 1 and 8 must be satisfied simultaneously to ensure the SL-ARROW-based confinement in the lateral direction. On the other hand, Eq. (2) indicates the condition to spoil the waveguiding in the lateral direction.

Thirdly, for 2D waveguiding, the light must also be confined vertically by the ML-ARROWs, and it is important to match their phase velocities or effective indices  $n_{eff}$  when integrating the SL- and ML-ARROWs. This can be done by fine-tuning  $\theta_l$  through adjusting  $w$ .

## 2.4 Design and Validation

### 2.4.1 Model Structure Design

As a validation of the 2D SL/ML-ARROW scheme and its LCW conditions, we designed one exemplary structure and analyzed it numerically to see the agreement. We assumed that the SL-ARROW ridges and the liquid-core were made of common polymer materials ( $n_s = 1.55$ ) and H<sub>2</sub>O ( $n_c = 1.33$ ). For ML-ARROW fabrication, we assumed the use of high index Si<sub>3</sub>N<sub>4</sub> ( $n_{mh} = 2.05$ ) and low index SiO<sub>2</sub> ( $n_{ml} = 1.46$ ) layers deposited on glass substrates ( $n_{sup}, n_{sub} = 1.45$ ). The target wavelength  $\lambda_o$  was 785 nm, near the onset of the biological window in which the optical absorption by water and scattering by protein molecules decrease simultaneously [13]. We also assumed that the electric field component of the mode is TE-polarized to the ML-ARROW. Then the ARROW equation [3] set  $d_{mh}$  and  $d_{ml}$  at 125 and 318 nm, respectively. Seven ML-ARROW layers were used on each side. The channel height was

set to  $h = 3 \mu\text{m}$ , which is typical in optofluidics due largely to mode size considerations [1,14-16].

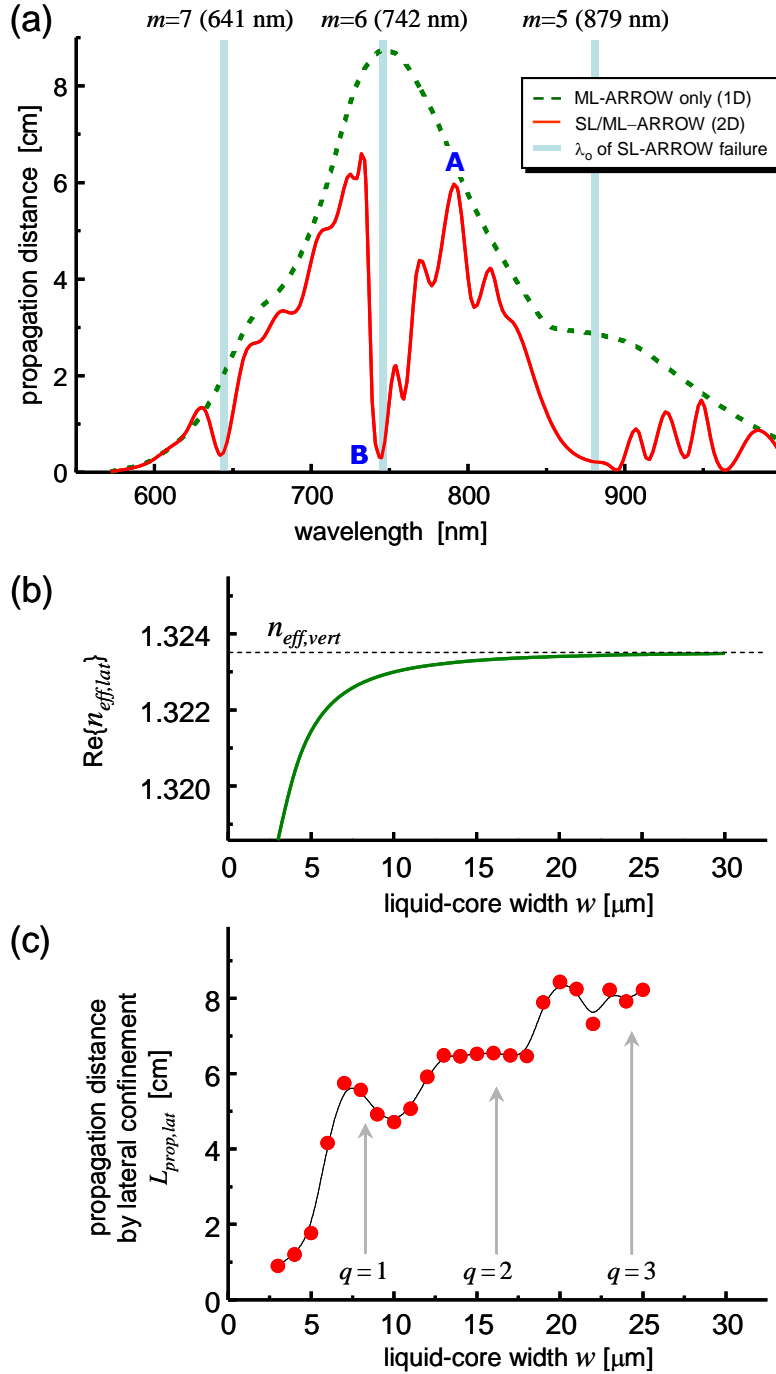


Figure 2.3 (a) The dotted and solid curves show the calculated values of  $L_{prop,vert}$ , the propagation distance owing only to the 1D ML-ARROW confinement, and  $L_{prop,2D}$ , the

combined result of ML/SL-ARROWS. Vertical bars mark the wavelengths at which the lateral confinement due to the SL-ARROW fails. (b) The curve shows the relation between the liquid-core width  $w$  and the real part of  $n_{eff,lat}$ , the effective index arising from the SL-ARROW-based lateral confinement, calculated by EIM/TMM. As the liquid-core widens,  $n_{eff,lat}$  increases monotonically, approaching the target value of  $n_{eff,vert}$ . (c) Unlike the monotonic increase in  $\text{Re}\{n_{eff,lat}\}$ ,  $L_{prop,2D}$  increases with substantial fluctuations as  $w$  widens. The arrows specify the values of  $w$  at which the condition of Eq. (8) is satisfied which relates the mode angle  $\theta_l$  and the ratio between  $\lambda_o/n_c$  and  $w$ .

First, the vertical confinement by the ML-ARROW was characterized by applying finite-element method [17] to the ML/H<sub>2</sub>O/ML structure specified above. For this, we set  $w = 12 \mu\text{m} \gg h$  to make the analysis quasi-1D.  $L_{prop,vert}$  was extracted from  $n_{eff,vert}$  and plotted in Figs. 2.3(a). It shows that the ML-ARROW-based vertical confinement is effective over a 120 nm 3 dB bandwidth around the target  $\lambda_o$ . The real part of  $n_{eff,vert}$  falls within 1.322 ~ 1.325 range. At the target  $\lambda_o$ , in particular,  $n_{eff,vert} = 1.3235$ . The shape and amplitude of the  $L_{prop,vert}$  curve can be optimized for the target  $\lambda_o$  by adjusting  $h$ .

With  $n_{eff,vert}$  fixed, we proceeded to optimize the integration of the lateral and vertical confinement mechanisms. We first used the anti-ARROW condition in Eq. (2) to shape the  $L_{prop}$  spectrum. Note that  $\varphi_{TIR}$  must be evaluated assuming a TM-polarized input this time. For the current design, we set  $d_s = 3 \mu\text{m}$  to place a dip near the center of the  $L_{prop,vert}$  peak (742 nm for  $m = 6$ ), resulting in a twin-peak under the envelope of the  $L_{prop}$  spectrum. The existence of dual transmission windows is useful for many optical sensing applications such as microfluidic fluorescence (FL) excitation and detection [1,2]. Note that for all of the calculations, the effective indices of the ridge ( $n_{s,eff} = 1.32353$ ) and the core ( $n_{c,eff} = 1.54084$ ),



which already incorporated the impact of the vertical confinement by the ML-ARROW, have been used.

Then, to satisfy the third condition, we tried to match  $\text{Re}\{n_{\text{eff},\text{lat}}\}$  to  $\text{Re}\{n_{\text{eff},\text{vert}}\}$ . Figure 2.3(b) shows  $\text{Re}\{n_{\text{eff},\text{lat}}\}$  calculated with effective index method (EIM) [18] and transfer matrix method (TMM) [19] at 785 nm. It shows that  $\text{Re}\{n_{\text{eff},\text{lat}}\}$  smoothly approaches  $\text{Re}\{n_{\text{eff},\text{vert}}\} = 1.3235$  as  $w$  increases. This suggests that, ideally, the integration of the ML- and SL-ARROWs must be increasingly better as  $w$  widens and, in accordance,  $L_{\text{prop},\text{lat}}$  must increase monotonically. But the  $L_{\text{prop},\text{lat}}$  curve, extracted from FEM simulation results shown in Fig. 2.3(c) does not exhibit such a monotonic increase. Instead, it exhibits fluctuations that must be considered to maximize  $L_{\text{prop}}$ . In fact, as shown in Fig. 2.3(c), the first three peaks in  $L_{\text{prop},\text{lat}}$  are close to the three  $w$  values (8.22, 16.44, and 24.66  $\mu\text{m}$ ) that satisfy the condition in Eq. (8) when the mode angle  $\theta_l$  was set to  $\text{asin}(\text{Re}\{n_{\text{eff},\text{lat}}\}/n_{\text{c,eff}})$ ,  $n_{\text{eff},\text{lat}} = 1.322$ , and  $q = 1\sim 3$ . Since  $n_{\text{eff},\text{lat}}$  itself changes with  $w$ , rigorous optimization requires scanning a range of  $w$  with numerical simulations using Eq. (8) as a guide. For structural and material parameters and target  $\lambda_o$  at 785 nm, the best configuration in terms of  $L_{\text{prop}}$  should be achieved at  $w \sim 7.5, 13, \text{ or } 20 \mu\text{m}$ .

#### 2.4.2 Numerical Validation

To confirm the results above, we performed 2D numerical analyses on the fundamental mode of the SL/ML-ARROW LCW using a fully-vectorial finite-element method [17]. The excellent agreement between the 2D FEM and the EIM/TMM results shown in Fig. 2.4(a) further validated our design procedure. The  $L_{\text{prop},2\text{D}}$  extracted from the 2D FEM results were superimposed in Fig. 2.3(a). Careful examination of the traces in Fig. 2.3(a) reveals that the

overall  $L_{prop,2D}$  is indeed constructed by burning holes into the  $L_{prop,vert}$  curve at wavelengths which satisfy  $\Delta\phi_l = (2m+1)\pi$ . The calculated  $L_{prop,2D}$  is approximately 6 cm which is comparable or longer than reported values [1,2].

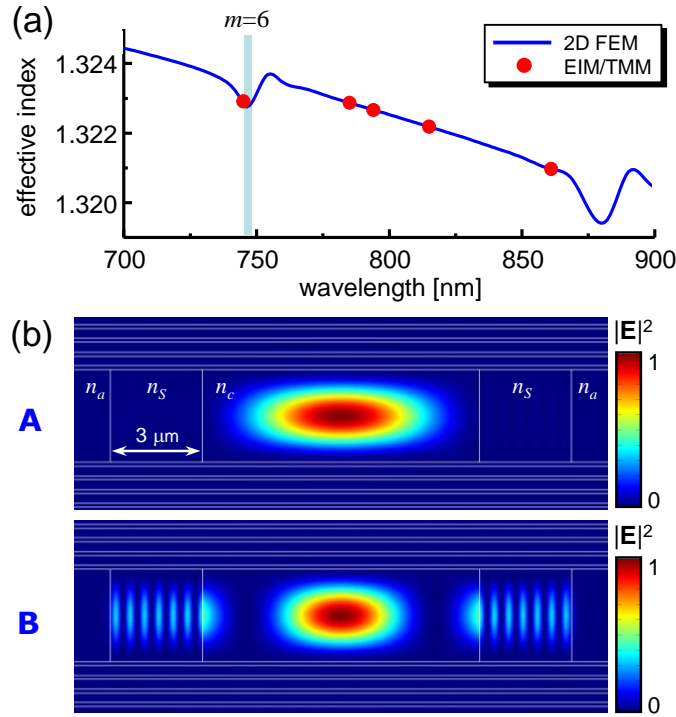


Figure 2.4 (a) Comparison of EIM/TMM and 2D vectorial FEM results. (b) Calculated profiles of the 2D LCW's fundamental mode at two different  $\lambda_o$  marked in Fig. 2.3(a).

The profiles of the fundamental mode were obtained at two points corresponding to a peak (**A**) and a dip (**B**) marked in Fig. 2.3(a) and plotted in Fig. 2.4(b). It is evident that at **B**, a significant portion of mode power is confined within the SL-ARROW ridges while the mode is well-confined within the liquid-core at **A**. Since the ML-ARROWs are designed for ML/H<sub>2</sub>O/ML, not ML/SL/ML, the mode power within the ridge will experience a higher level of leakage, exhibiting higher propagation loss. This loss due to the combined failure in ARROW integration does not show up in the EIM/TMM calculation and can only be

estimated by numerical modal analyses. The numerical analysis also identified only one higher order mode within the liquid-core. Its effective index was  $1.32088 - i \cdot 1.4984 \times 10^{-6}$ , indicating  $L_{prop,2D}$  close to 86% of that of the fundamental mode, or 5.2 cm. Since the second mode assumes a double-peak mode profile, the low overlap integral with the single-peak fundamental mode will prevent its generation through modal coupling. To the delivery of optical power, the existence of a higher order mode with comparable propagation distance is not detrimental either. The two liquid-core modes described so far have their electric fields polarized in  $y$ -direction. Each of them was accompanied by an  $x$ -polarized mode whose effective index is very close to the  $y$ -polarized mode in the real part but is more than 200 times higher in the imaginary part. The consequential reduction in  $L_{prop,2D}$  renders their existence insignificant.

#### 2.4.3 Optimization and Application

The design procedures established and validated in the previous sections can be utilized to optimize or tailor the transmission characteristics of the ML/SL-ARROW. As the first example, we tried to further optimize the model structure designed in the previous section.

Firstly, we tried to tailor the  $L_{prop,2D}$  curve in Fig. 2.3(a) so that it would exhibit a single-peak near  $\lambda_o = 750$  nm around which the  $L_{prop,vert}$  due to ML-ARROW reaches its peak. Based on Eq. (2), we increased  $d_s$  to  $3.3 \mu\text{m}$  to red-shift the dips by approximately 50 nm. The resulting  $L_{prop,2D}$  curve shown in Fig. 2.5(a) indicates that the dips were indeed shifted as expected, positioning the  $L_{prop,vert}$  peak between the two dips corresponding to  $m = 6$  and 7.

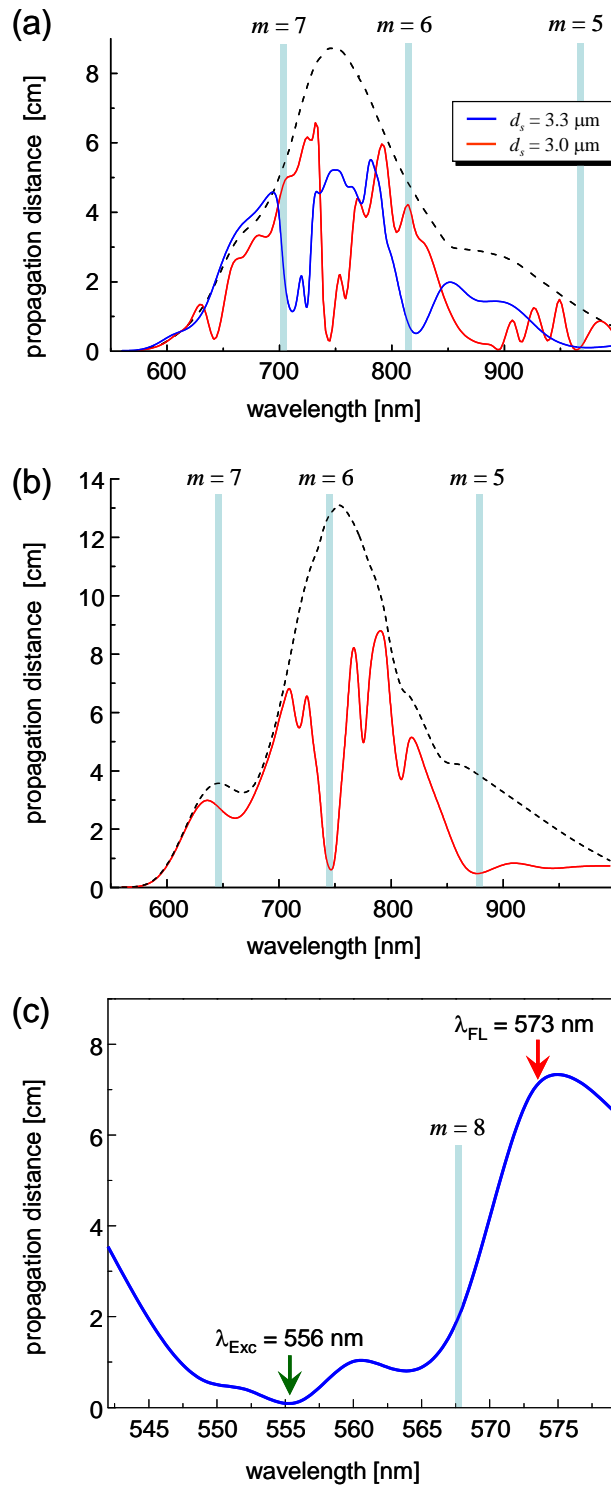


Figure 2.5 (a)  $L_{prop,2D}$  curve as a function of  $\lambda_o$  when  $d_s$  was increased to  $3.3 \mu\text{m}$ . The vertical bars mark the new  $\lambda_o$  values at which the SL-ARROW-based lateral confinement fails. The

$L_{prop,2D}$  curve for  $d_s = 3.0 \mu\text{m}$  is also superimposed for comparison. It indicates that the increase in  $d_s$  red-shifts the  $L_{prop,2D}$  dips, making the  $L_{prop,2D}$  profile single-peaked near  $\lambda_o \sim 750 \text{ nm}$ . (b)  $L_{prop,2D}$  curve for a ML/SL-ARROW for which  $d_s$  and  $w$  were maintained at 3.0 and 9.0  $\mu\text{m}$  but  $h$  was increased to 3.3  $\mu\text{m}$ . The increase in the vertical confinement itself has led to an augmented  $L_{prop,2D}$ . (c) Another  $L_{prop,2D}$  curve for a ML/SL-ARROW designed for the optofluidic excitation and detection of Alexa Fluor 546 dye.

It also shows that, however, the  $>8 \text{ cm}$  peak value in  $L_{prop,vert}$  did not become available in the case of the combined ML/SL-ARROW scheme, making  $L_{prop,2D}$  saturated at approximately 6 cm. As an alternative approach, we kept the configuration for the lateral confinement intact and tried to improve the vertical confinement so that the envelope itself could be raised. For operation  $\lambda_o \sim 785 \text{ nm}$ , the maximum in  $L_{prop,2D}$  was achieved when  $h$  was increased to 3.3  $\mu\text{m}$ , which is approximately 10% off from the design value of the 1D ARROW equation [3]. We attribute the discrepancy to the conversion from 1D to 2D confinement. As shown in Fig. 2.5(b),  $L_{prop,2D}$  at 785 nm was increased to 8.55 cm. Again, the dips in the  $L_{prop,2D}$  curve occurred exactly at the  $\lambda_o$  values calculated with Eq. (2) using the  $n_{s,eff}$  and  $n_{c,eff}$  recalculated for  $h = 3.3 \mu\text{m}$ .

As an additional example, we designed an optofluidic waveguide optimized for excitation and detection of the FL from Alexa Fluor 546 dye which absorbs light at 556 nm and emits FL at 573 nm. Since the suppression of the residual excitation is a critical factor in determining the FL detection performance, it is important to place the  $L_{prop}$  dip at the excitation wavelength while maintaining its peak at the FL wavelength. For this, we first set  $d_{mh}$  and  $d_{ml}$  at 125 and 235 nm, respectively, to shift the  $L_{prop,vert}$  curve toward the spectral regime of interest. We then fixed  $h$  at 3  $\mu\text{m}$  and adjusted  $d_s$  and  $w$  to position the  $L_{prop}$  dip at

556 nm and the peak at 573 nm. The dip-position estimation based on Eq. (2) suggested that a dip corresponding to  $m = 8$  would be positioned near 560 nm when  $d_s \sim 3 \mu\text{m}$ . Further 2D FEM simulations with varying values of  $w$  revealed that when  $w \sim 12 \mu\text{m}$ , the minimum in  $L_{prop}$  can be placed at 556 nm with a matching peak near 575 nm, as shown in Fig. 2.5(c). This type of twin-peak spectral response will greatly facilitate the realization of chip-scale FL biosensors in the future.

#### 2.4.4 Impact of Structural Parameters

We have also performed parametric studies on the sensitivity of the ML/SL-ARROW's waveguiding performance to potential fabrication imperfections. We identified three major sources of imperfections. First, the error in  $h$ , the channel height, can be generated while adding an adhesive layer between the SL-ARROW's top-surface and the ML-ARROW's bottom-surface for their attachment. The instability in the spin-coating process can also introduce uncertainties to  $h$ . Furthermore, fabrication imperfections can occur to the widths of the SL-ARROW ( $d_s$ ) and the liquid-core ( $w$ ). While the positions of the two ridges can be accurately controlled during the photolithography process, their width may vary depending on the conditions of the development process. In this case,  $w$  and  $d_s$  must be considered in combination since an increase in the former automatically results in a decrease in the latter, and *vice versa*. Through 2D numerical mode analyses, we calculated the changes in  $L_{prop,2D}$  at 785 nm resulting from the imperfections in  $d_s$ ,  $w$ , and  $h$  in the range of  $< \pm 10\%$ . The results are shown in Table 1. First of all, they indicate that substantial increase or decrease in  $L_{prop,2D}$  due to errors in the length-scale of 100~200 nm and the fabrication process must be controlled accordingly. We attributed some abrupt changes in  $L_{prop,2D}$  to the ripples in the

$L_{prop,2D}$  spectral curves shown in Figs. 2.3(a), 2.5(a), and 2.5(b). On the other hand, the results also indicate that such variations in the structural parameters can be used to maximize  $L_{prop,2D}$ . At 785 nm, the longest  $L_{prop,2D}$  was 9.94 cm obtained from  $d_s = 2.9 \mu\text{m}$ ,  $w = 9.1 \mu\text{m}$ , and  $h = 3.3 \mu\text{m}$ .  $L_{prop,2D}$  begins to decline beyond  $h = 3.3 \mu\text{m}$ .

Table 2.1  $L_{prop,2D}$  (in cm) obtained from 2D numerical mode analyses using different combinations of the structural parameters  $d_s$ ,  $w$ , and  $h$  values (all in  $\mu\text{m}$ ). Due largely to the ripples in the  $L_{prop,2D}$  spectral curves shown in Figs. 2.3 and 2.5, the values exhibit substantial changes corresponding to variations in the structural parameters in the length scale of 100 nm. The best result was obtained when  $d_s = 2.9 \mu\text{m}$ ,  $w = 9.1 \mu\text{m}$ , and  $h = 3.3 \mu\text{m}$ .

$d_s / w \backslash h$	2.7	2.85	3	3.1	3.2	3.3	3.4
2.7/ 9.3			2.09	2.73	3.00	3.05	2.41
2.8/ 9.2			6.27	9.03	9.35	9.37	8.42
2.9/ 9.1			5.80	8.85	8.85	9.94	9.28
3.0/ 9.0	3.29	5.00	5.05	5.54	7.99	8.55	8.04
3.1/ 8.9			1.43	1.22	1.76	2.67	2.91
3.2/ 8.8			0.81	0.86	0.95	0.99	1.03
3.3/ 8.7			3.80	5.12	5.62	5.83	5.73

#### 2.4.5 Dual-Use of SL-ARROW

Figure 2.6(a) shows the profile of the fundamental mode supported by the SL-ARROW ridge. Figure 2.6(b) portrays the evanescent tail of the mode into the liquid-core. The  $e^{-1}$  penetration depth was 157 nm. This solid-core waveguide can be utilized for evanescent optical sensing and delivery of optical waves to arbitrary points of the LCW network.

## 2.5 Conclusion

In conclusion, we proposed a new LCW scheme which utilizes two different types of ARROW schemes in combination, *i.e.*, an SL-ARROW for lateral confinement and the conventional ML-ARROW for the vertical confinement. Such an integrated scheme will enable a simpler, soft-lithography-based fabrication and will fortunately be accompanied by built-in solid-core waveguides. Taking advantage of the orthogonal nature of their integration, we derived a set of simple rules to optimize the new LCW scheme.

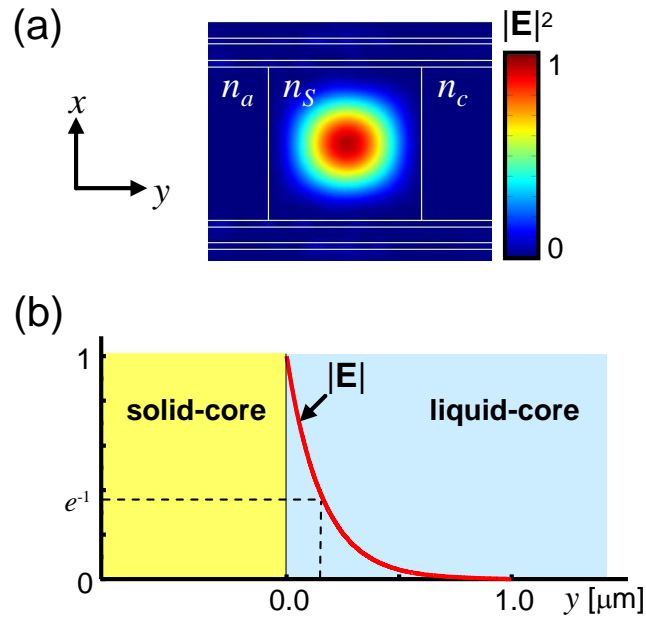


Figure 2.6 (a) The calculated profile of the mode supported by the SL-ARROW ridge. (b) The decay of  $|E|$  into the liquid-core.

It was revealed that the overall spectral shape in terms of the propagation distance can be initially set using the conventional ARROW equation while further optimization can be achieved through a rough estimation based on the condition derived in this paper and fine-adjustments through 2D numerical analyses. The 2D simulation results exhibited excellent



agreements with the theoretical estimations and conditions. Based on the process, we numerically demonstrated 6~10 cm of propagation distance from model LCWs with typical dimensions.

## 2.6 Acknowledgement

JL and JK were supported by NSF CAREER award (0954845). ZY and KMH were supported by Director for Energy Research, Office of Basic Energy Sciences. The Ames Laboratory is operated for the U.S. Department of Energy by Iowa State University under contract No. W-7405-Eng-82.

## 2.7 References

- [1] H. Schmidt and A. R. Hawkins, "Optofluidic waveguides: I. Concepts and implementations," *Microfluid. Nanofluid.* **4**, 3-16 (2008).
- [2] A. R. Hawkins and H. Schmidt, "Optofluidic waveguides: II. Fabrication and structures," *Microfluid. Nanofluid.* **4**, 17-32 (2008).
- [3] T. L. Koch, U. Koren, G. D. Boyd, P. J. Corvini, and M. A. Duguay, "Antiresonant reflecting optical waveguides for III-V integrated optics," *Electron. Lett.* **23**, 244-245 (1987).
- [4] S. Campopiano, R. Bernini, L. Zeni, and P. M. Sarro, "Microfluidic sensor based on integrated optical hollow waveguides," *Opt. Lett.* **29**, 1894-1896 (2004).
- [5] D. Yin, D. W. Deamer, H. Schmidt, J. P. Barber, and A. R. Hawkins, "Single-molecule detection sensitivity using planar integrated optics on a chip," *Opt. Lett.* **31**, 2136-2138 (2006).

- [6] I. V. Goltser, L. J. Mawst, and D. Botez, "Single-cladding antiresonant reflecting optical waveguide-type diode laser," *Opt. Lett.* **20**, 2219-2221 (1995).
- [7] N. M. Litchinitser, A. K. Abeeluck, C. Headley, and B. J. Eggleton, "Antiresonant reflecting photonic crystal optical waveguides," *Opt. Lett.* **27**, 1592-1594 (2002).
- [8] E. J. Lunt, P. Measor, B. S. Phillips, S. Kuhn, H. Schmidt, and A. R. Hawkins, "Improving solid to hollow core transmission for integrated ARROW waveguides", *Optics Express*, **16**, 20981-20986 (2008).
- [9] H. P. Uranus, H. J. W. M. Hoekstra, and E. van Groesen, "Consideration on material composition for low-loss hollow-core integrated optical waveguides," *Opt. Comm.* **260**, 577-582 (2006).
- [10] T. Delonge and H. Fouckhardt, "Integrated optical detection cell based on Bragg reflecting waveguides," *J. Chromatography A*, **716**, 135-139 (1995).
- [11] O. Schmidt, M. Bassler, P. Kiesel, N. M. Johnson, and G. H. Döhler, "Guiding light in fluids", *Applied Physics Letters*, **88**, 151109 (2006).
- [12] G. R. Fowles, Introduction to modern optics (Dover, New York, 1975).
- [13] A. Vogel and V. Venugopalan, "Mechanisms of Pulsed Laser Ablation of Biological Tissues," *Chem. Rev.* **103**, 577-644 (2003).
- [14] P. Dumais, C. L. Callender, C. J. Ledderhof, and J. P. Noad, "Monolithic integration of microfluidic channels, liquid-core waveguides, and silica waveguides on silicon," *Appl. Opt.* **45**, 9182 – 9190 (2006).
- [15] G. L. Liu, J. Kim, Y. Lu, and L. P. Lee, "Optofluidic control via photothermal nanoparticles," *Nature Materials*, **5**, 27-32 (2006).

- [16] Z. Li and D. Psaltis, "Optofluidic distributed feedback dye lasers," *IEEE J. Selected Topics in Quantum Electronics*, **15**, 185- 193 (2007).
- [17] Comsol Multiphysics (Comsol Inc. Waltham, MA).
- [18] G. B. Hocker and W. K. Burns, "Mode dispersion in diffused channel waveguides by the effective index method," *Appl. Opt.* **16**, 113-118 (1977).
- [19] K. H. Schlereth and M. Tacke, "The complex propagation constant of multilayer waveguides: an algorithm for a personal computer," *IEEE J. Quantum Electron.* **26**, 627-630 (1990).

## **CHAPTER 3. Fabrication of strongly anchored, ultrahigh aspect-ratio elastomeric microwires for mechanical and optical applications**

Modified from a paper published in *Journal of Micromechanics and Microengineering*

Jiwon Lee and Jaeyoun Kim\*

### **3.1 Abstract**

We present a new technique for fabricating microwires with high elasticity and aspect-ratio. Thanks to the adoption of lost-wax casting in the fabrication, the microwires can be directly *grown* from their supporting structure in the out-of-plane, surface-normal direction, automatically accomplishing strong, monolithic anchoring. The microwires can also be anchored at both ends in an arrayed format, making themselves more useful for mechanical and optical applications. Using the new technique, we fabricated arrays of PDMS microwires 150 to 250  $\mu\text{m}$  thick and 2 to 20 mm long. The microwires can withstand  $>400\%$  elongations and  $>70$  mN of pulling force with little degradation in their surface smoothness. Optical characterizations revealed that the PDMS microwires can function as flexible lightpipes connecting two points in miniaturized systems.

### **3.2 Introduction**

There have been growing demands for microwires with high elasticity and aspect-ratio in various fields of small-scale technology. In MEMS actuators, they can function as a spring element which stores mechanical energy and releases it abruptly. Such a capability has been utilized for producing jumping [1] or flapping [2] motions in microrobots. When made of

optically transparent materials, they can also function as optical jump-wires for exchanging optical power and signals to and from hard-to-reach locations in densely packed assemblies, such as backplane-plugged circuit boards [3] or optofluidic devices [4]. They will be especially useful for mimicking biological optical systems in which flexible fibers frequently play an essential role as the conduit of optical signals [5].

A variety of schemes have been proposed to fabricate such microwires. They include drawing [6-10], electro-spinning [11-13], soft lithography [14], photo-polymerization [15], and self-writing [16]. Most schemes produce highly flexible, often elastic, nano- to micro-scale wires. Explicit optical transmission measurements have also been performed on some microwires made of transparent materials [6,7,16].

One important issue which has often been overlooked in those schemes is the need to anchor the fabricated microwires. For a full utilization of the microwire's elasticity, at least one of its ends must be anchored firmly to an external supporting structure. Anchoring is also essential for forming patterned arrays of microwires and integrating them with other functional blocks. Moreover, some important applications, such as the spring action or optical jump-wiring, require the microwires be anchored at both ends, or *doubly-anchored*. Particularly for the optical applications, the anchoring site needs to double as a terminal for coupling light in and out of the microwires.

Many of the existing fabrication schemes, however, produce microwires in highly coiled or entangled forms, making their anchoring very difficult [11-13,15]. Some of the microwires feature built-in anchoring but their anchoring strengths have not been characterized [8-10]. More importantly, all the doubly-anchored microwires demonstrated so far run in parallel to

their substrates, rather than along the out-of-plane, surface-normal direction which will be of greater use for many of the applications stated above.

Recently we proposed to *grow* microwires directly from their supporting structure, thus automatically realizing a *monolithic* anchoring which is inherently robust, surface-normal, and optically transmissive. The results of preliminary fabrication and mechanical characterizations can be found in Ref. [16]. In this paper, we present more details on the fabrication process, including the impact of our efforts to improve the yield and results of further morphological and optical characterizations.

### 3.3 Fabrication Principle and Details

The fabrication process flow is illustrated in Fig. 3.1. It basically is a two-step, transition mold-mediated replication of metallic microwires with elastomer. This technique bears certain similarity to the ubiquitous lost-wax casting which has already been adopted for MEMS fabrication previously [17]. In the first stage (Figs 3.1a-1e), a transition mold with cylindrical openings is fabricated. In the second stage (Figs 3.1f-1i), liquid-phase (LP) elastomer is poured over the transition mold to flow down the openings, forming elastomeric microwires connected monolithically to the bulk of elastomer above the transition mold after solidification. If allowed to flow through the openings, the LP elastomer can form another structure beneath the mold, producing doubly-anchored microwires. The monolithic nature of this anchoring ensures robust and optically clear interface between the supporting structures and the microwires. The protocol's compatibility with conventional soft lithographic techniques also facilitates the microwires' functional and structural integration with other polymer MEMS and microfluidic devices.

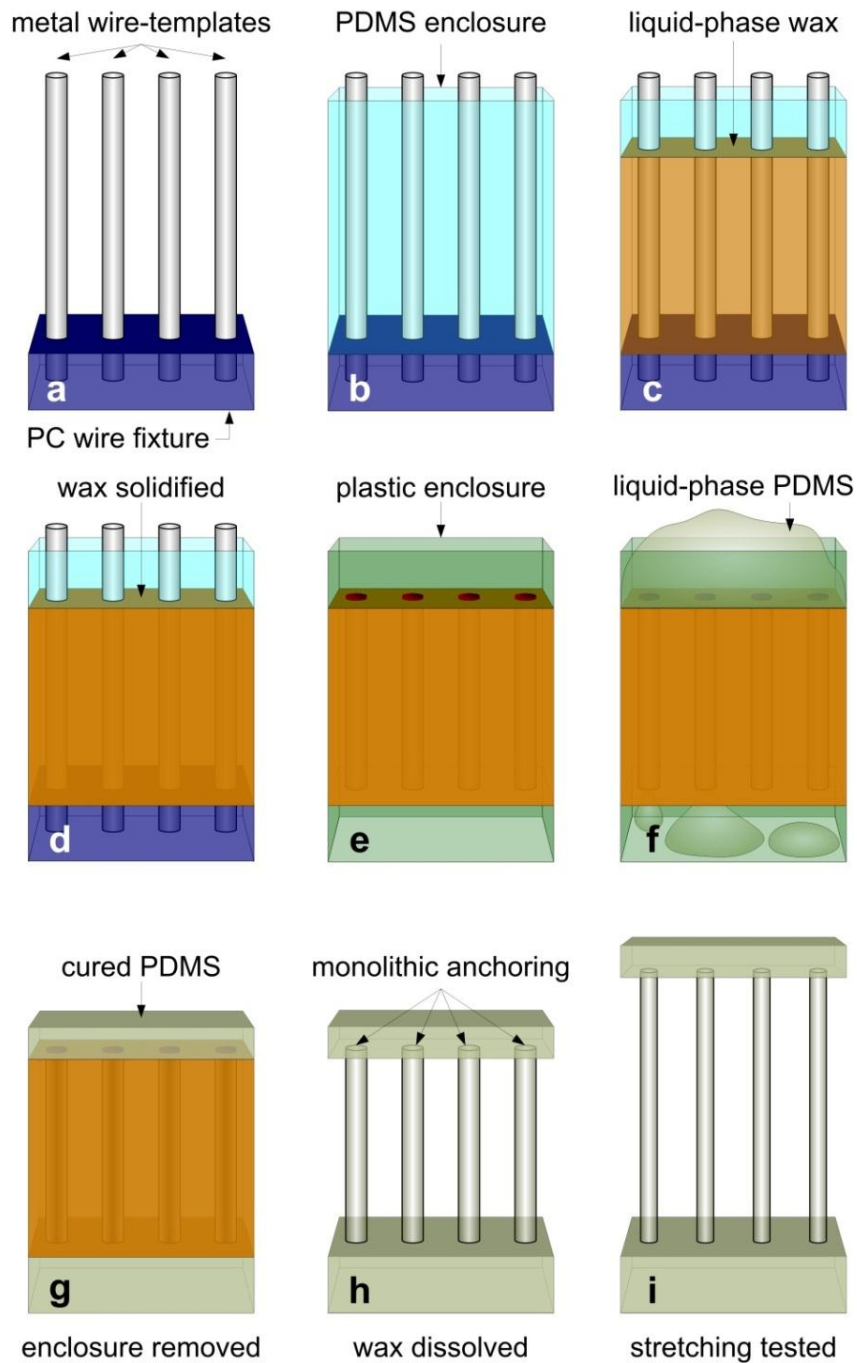


Figure 3.1 The process flow for the fabrication of monolithically anchored elastomeric microwires: (a) Preparation of a patterned array of wire-templates, (b-e) The first replication to make a transition mold, (f-g) The second replication with PDMS, and (h-i) Release and testing of the microwire's tensile characteristics.

As the elastomer, we chose poly(dimethylsiloxane) (PDMS) for its excellent elasticity, optical clarity, and ease of handling. It is also a proven material for fabricating microfluidic and micro-optic components. One potential drawback of PDMS is its tendency to swell and deform upon contacting solvents. To prevent the adverse effect, we made the sacrificial transition mold with a water-soluble material. Among a variety of such materials, including polyethylene glycol [18,19], polyvinyl alcohol [20,21], and water-soluble wax [22], we chose the last one mainly for its supreme replication fidelity and surface quality.

The fabrication process began with preparing a wire fixture by drilling a patterned array of holes into a polycarbonate substrate. The holes were then planted with straightened steel wires (from Smallparts Inc.) which will function as the microwire templates. Then the wire-template/substrate assembly was placed within a PDMS enclosure. Next the LP water-soluble wax (Freeman Optical Inc.), which has been heated for 5 hours at 105°C, was poured into the enclosure. Only the transparent portion of the LP wax was separated and used. To prevent defect formation, the LP wax must be poured slowly into the PDMS enclosure and a PDMS lid was placed on the top. Once the wax transition mold solidified completely, the wire-template/fixture and the PDMS enclosure were removed manually. Before this removal, the whole structure was placed on a 45°C hot-plate for 20 minutes. In the second replication step, the wax mold was placed within a plastic enclosure, and a LP mixture of PDMS and its curing agent was poured from the top of the transition mold. PDMS base (Sylgard 184) and curing-agent were mixed at 10:1 ratio, stirred for 10 minutes, and degassed before pouring. Initially, this step was a major source of fabrication failure since the flow of LP PDMS often stopped in the middle the holes. Air trapping inside the holes could also cause irregularities along the length of completed mirowires. This was especially frequent when the aspect ratio



exceeds 10:1. By applying vacuum from the substrate side, we could force the flow of the LP PDMS and ensure a complete filling. This increased the yield significantly. The whole setup was then placed on a hot plate for thermal curing. Controlling the curing temperature was critical to promoting PDMS cross-linking without deforming the wax transition mold. We cured the whole structure for 24 hours at a low temperature ( $\sim 40^{\circ}\text{C}$ ) to prevent the possible reflow of the wax.

Once the PDMS was completely cured, we peeled off the plastic enclosure from the wax/PDMS composite and dissolved the wax with warm water at  $50^{\circ}\text{C}$ . Upon complete dissolution of the wax, we fished out the completed PDMS microwires from water. This step was another major source of fabrication failure since the surface tension of water was often strong enough to pull and break the microwires. Consequentially, the failure rate increased for thinner microwires. We overcame this difficulty by adding surfactant to the water to reduce the surface tension. We chose ethanol as our surfactant and added it to the water as a 8:2 ratio. This lowered the surface tension from that of pure water (67.9 mN/m) to the level of ethanol (23.3 mN/m) [23]. This process was carried out right before the microwires was lifted out of water to minimize the impact of ethanol to PDMS. The ethanol surfactant, however, becomes ineffective for microwires with diameter  $< 130\ \mu\text{m}$ . Currently this difficulty associated with surface tension is the most significant limiting factor in further miniaturization of the microwire. The final structure was then dried in room temperature.

Overall, current success rate is about 96~97%. The highest aspect ratio achieved so far is 80:1 obtained from a  $250\ \mu\text{m}$ -diameter, 2 cm-long microwire.

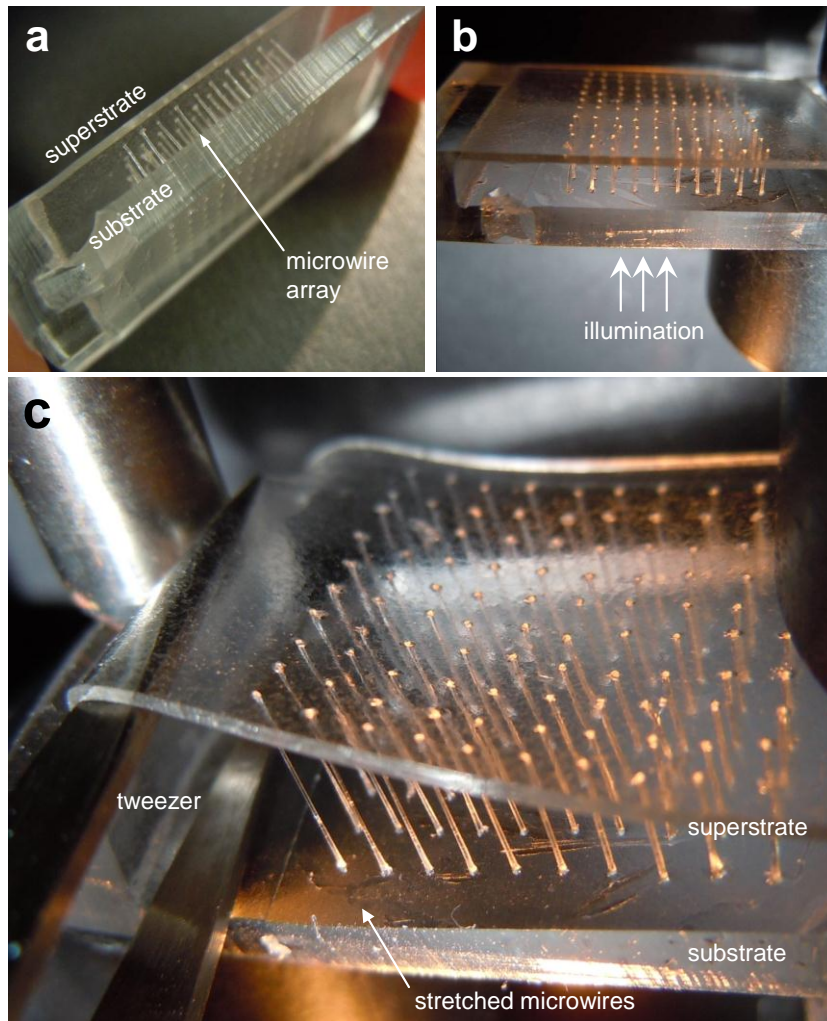


Figure 3.2 (a) A 10x10 array of 150  $\mu\text{m}$ -diameter, 2.5 mm-long doubly-anchored PDMS microwires. (b) The microwires exhibit excellent lightpipe characteristics. (c) When stretched by a pair of tweezers, the microwires withstood  $>300\%$  elongation.

### 3.4 Structural Characteristics

A large variety of microwire assemblies can be realized by varying the dimensions of the wire-template, the hole pattern, and the shape of the external supporting structure. As an example, Fig. 3.2a shows a 10 $\times$ 10 array of 150  $\mu\text{m}$ -diameter, 2.5 mm-long microwires vertically connecting two PDMS slabs with monolithic anchoring at both ends. The wire-to-

wire separation is 1 mm. The PDMS slab thicknesses are 1 and 3 mm, respectively. These can be varied by adjusting the enclosure dimensions and/or the quantity of LP PDMS. The microwires exhibited notable optical transparency and elasticity as shown in Figs. 3.2b and 3.2c, routinely withstanding >300% elongations.

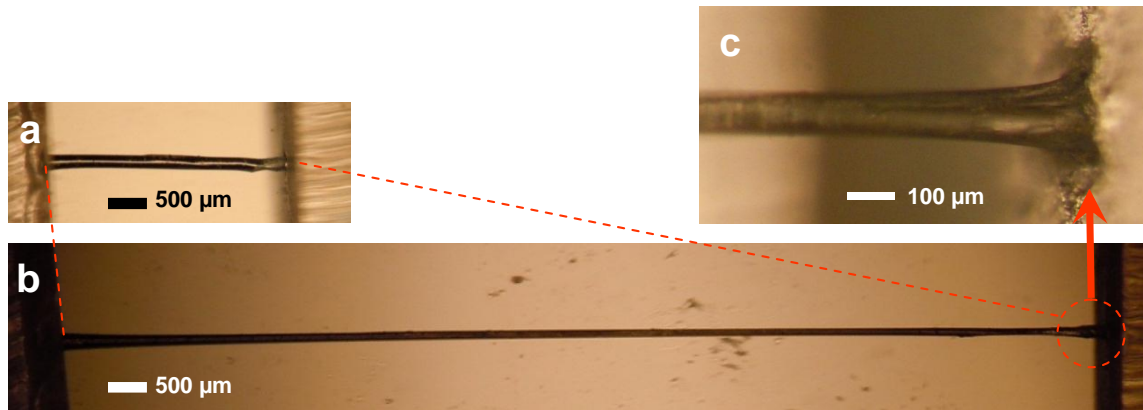


Figure 3.3 Microscope images of a 170  $\mu\text{m}$ -diameter, 2.5 mm-long microwire (a) before and (b) during a 440% elongation. (c) A further magnified image of the anchoring site under stretching (the circled area in (b)).

Figures 3.3a and 3.3b show the microscope images of a microwire before and during a 440% elongation, respectively. As the length of the microwire was increased from 2.5 to 11 mm, the waist diameter was reduced from 170  $\mu\text{m}$  to 79  $\mu\text{m}$ . The fact that a 440% elongation incurred less than 5% change in the structure's volume indicates that the deformation was hydrostatic [24,25]. Figure 3.3c is a magnified view of the anchoring site under stretching. It shows that the anchoring site becomes funnel-shaped as the middle part of the microwires gets thinner. The flaring angle is thus a function of elongation and becomes an important factor in optical applications, as will be shown in the next section.

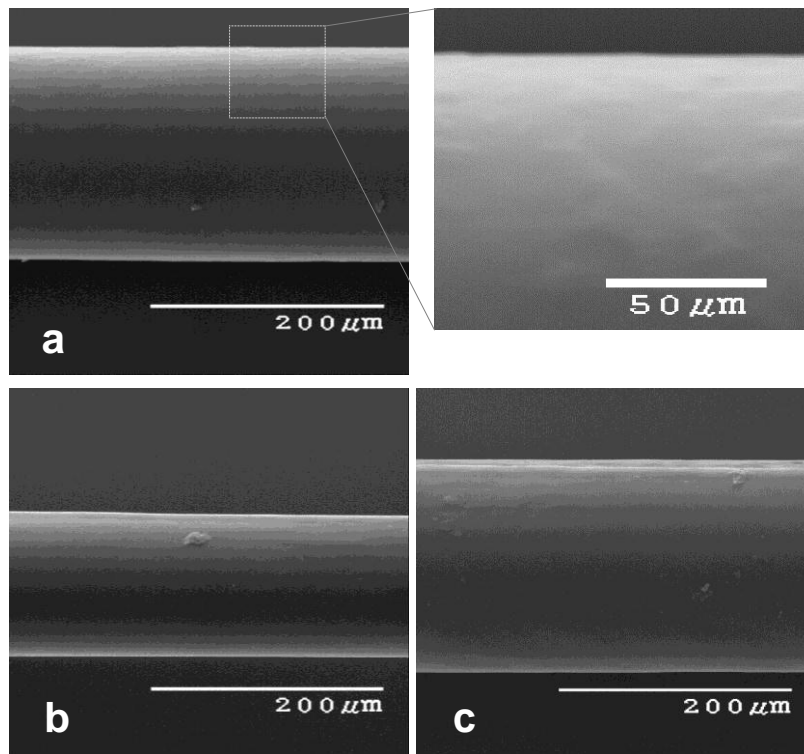


Figure 3.4 SEM images of a microwire (a) before (181  $\mu\text{m}$  at the waist) and (b) during a 300% elongation (118  $\mu\text{m}$  at the waist). (c) The surface of the same microwire after 25 cycles of 300% elongations. The inset of (a) shows the surface quality at a higher magnification.

To investigate the impact of the stretching on the microwires' surface quality, we took SEM scans of a 184  $\mu\text{m}$ -diameter PDMS microwire. Figure 3.4a shows the SEM image of the microwire. Its inset shows a further magnified image of the microwire's surface. The surface of the microwire fabricated through the lost-wax casting technique was smooth in micron-scale. The SEM images of the microwire during and after 25 cycles of 300% elongation are shown in Fig. 3.4b and 3.4c, respectively.

After the 25 cycles of elongation, the diameter of the microwire was permanently reduced from 184 to 181  $\mu\text{m}$ , which corresponds to a  $< 2\%$  change. Under the assumption of hydrostatic deformation [24,25], the resulting permanent change in the length of the

microwire is approximately 84  $\mu\text{m}$ . Due to the PDMS microwire's highly elastic nature, it was difficult to confirm this length change experimentally.

The surface smoothness was maintained after the 25 cycles of elongation, as shown in Fig. 3.3c, except for the formation of a few defects and longitudinal stretch marks. The formation of permanent wrinkles in the vertical direction, reported in some elastomeric microstructures [26], has not been observed.

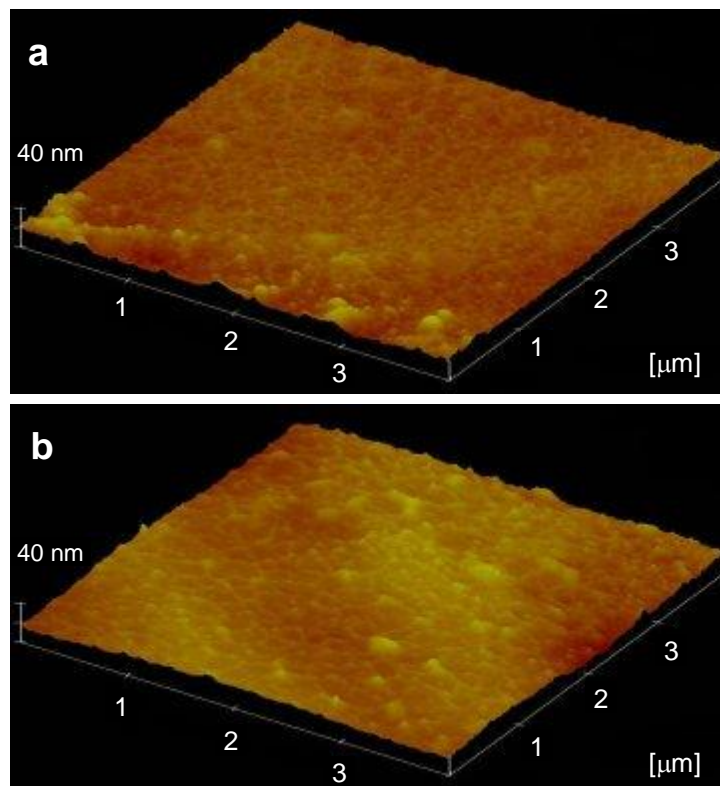


Figure 3.5 AFM images obtained by scanning over a  $16 \mu\text{m}^2$  area of the surface of a PDMS microwire (a) before and (b) after 25 cycles of 400% stretching.

The microwire's surface roughness was further characterized with atomic force microscopy (AFM). A typical 8 mm-long and 188  $\mu\text{m}$ -diameter PDMS microwire was used as the sample. 3D AFM scans of a  $16 \mu\text{m}^2$  area of the microwire's surface before and after 25

cycles of 400% stretching are shown in Figs. 3.5a and b, respectively. Before the stretching cycles, the root mean square roughness value obtained from 7 measurements was  $3.2 \pm 0.8$  nm. Sixteen measurements taken after the stretching resulted in a root mean square roughness of  $3.0 \pm 0.9$  nm, indicating negligible change in the roughness.

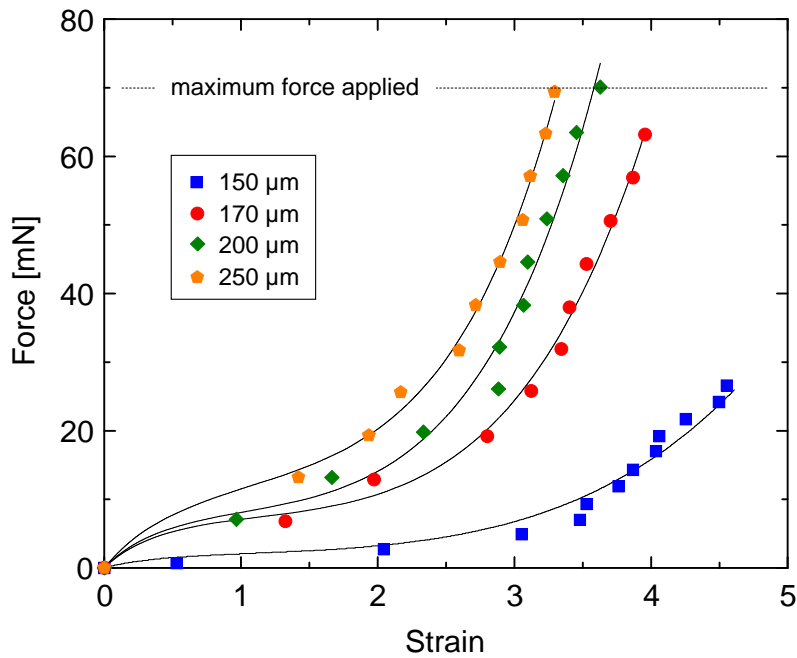


Figure 3.6 The force-strain curves of the four characterized microwires. The symbols represent the measurements and the super-imposed curves show the results of curve-fitting to the Ogden model.

### 3.5 Tensile Properties

We investigated the tensile properties of the PDMS microwires using a set of 2.5 mm-long microwires with four different values of diameters (150, 170, 200, and 250  $\mu\text{m}$ ). They were fabricated in one batch, and we paid close attention to maintain uniform process conditions because the mechanical properties of PDMS structures are strongly affected by their cross-linking conditions [27-29]. The microwires were stretched by adding weights to

the substrate while their top portions were held by a fixture. The elongation was measured using a computer-controlled micromanipulator,

The microwires with 150 and 170  $\mu\text{m}$  in diameter withstood 27 and 64 mN of stretching force before their failures, respectively. On the other hand, those with 200 and 250  $\mu\text{m}$  in diameter did not fail even when the force was increased to 70 mN, the maximum force tested. The failure always occurred at the waists rather than at either of the anchoring sites, indicating that the anchoring strength is greater than the maximum force withstood by the respective microwire. The measurement results are summarized in the force-strain plot in Fig. 3.6. The strain  $\varepsilon = \Delta l/l_o$  where  $\Delta l$  is the elongation and  $l_o$  the initial length. Figure 3.6 also shows that the tensile characteristics of the microwires agreed excellently with the Ogden model [30,31] which describes the force-strain relations of structures with highly nonlinear elasticity. Under a uniaxial stretching, the Ogden model dictates that

$$f = \mu_1 \left[ a^{\alpha_1 - 1} - a^{-\left(1 + \frac{1}{2}\alpha_1\right)} \right] + \mu_2 \left[ a^{\alpha_2 - 1} - a^{-\left(1 + \frac{1}{2}\alpha_2\right)} \right] \quad (1)$$

where  $f$  is the force,  $a = (l_o + \Delta l)/l_o = 1 + \varepsilon$ , and  $\mu_{1,2}$  and  $\alpha_{1,2}$  are the four curve-fitting parameters [30,31]. The Young's modulus  $E$  of the material can also be determined from the model as  $E = \mu_l \alpha_l$  where  $\mu_l$  and  $\alpha_l$  belong to the term which mainly affect the low strain ( $\varepsilon < 1$ ) portion of the force-strain response. The computed  $E$  values were 201, 564, 449, and 339 kPa for diameter values of 150, 170, 200, and 250  $\mu\text{m}$ , respectively. These are all within or close to the range of  $E$  values of the PDMS cured in low temperature (300~600 kPa for ~40°C curing temperature) reported in literature [27,28], further corroborating the

experimental results. The spring constant  $k$  of the microwires can be calculated from  $k = E \cdot A_o / l_o$  where  $A_o$  is the initial cross-sectional area. The estimated spring constant of the 170  $\mu\text{m}$ -diameter microwire is 5.1 N/m. The maximum elastic potential energy per volume in the microwire reaches to 0.85  $\text{mJ}/\text{mm}^3$  when  $\Delta l = 9.5 \text{ mm}$  (450% elongation). These characteristics are important in determining the microwire's usefulness as a spring or energy storage element. The values of spring constant and volume energy density obtained from our samples are comparable to those of another type of PDMS wire produced by a totally different protocol [1].

### 3.6 Optical Properties and Application

We also characterized the PDMS microwire as a conduit of optical signal and power. We first measured the propagation loss of the microwire. The initial measurement was made by comparing the optical throughput values obtained before and after cutting back a microwire. We took a 184  $\mu\text{m}$ -diameter, 2 cm-long microwire and cut it back by 1 cm. The estimated propagation loss was 3.5 dB/cm. The cut-back method, however, involves too much uncertainty and is not repeatable. To double-check the result, we performed another set of measurements using a different approach. As shown in Fig. 3.7a, we measured the changes in optical throughput as we elongate the microwire.



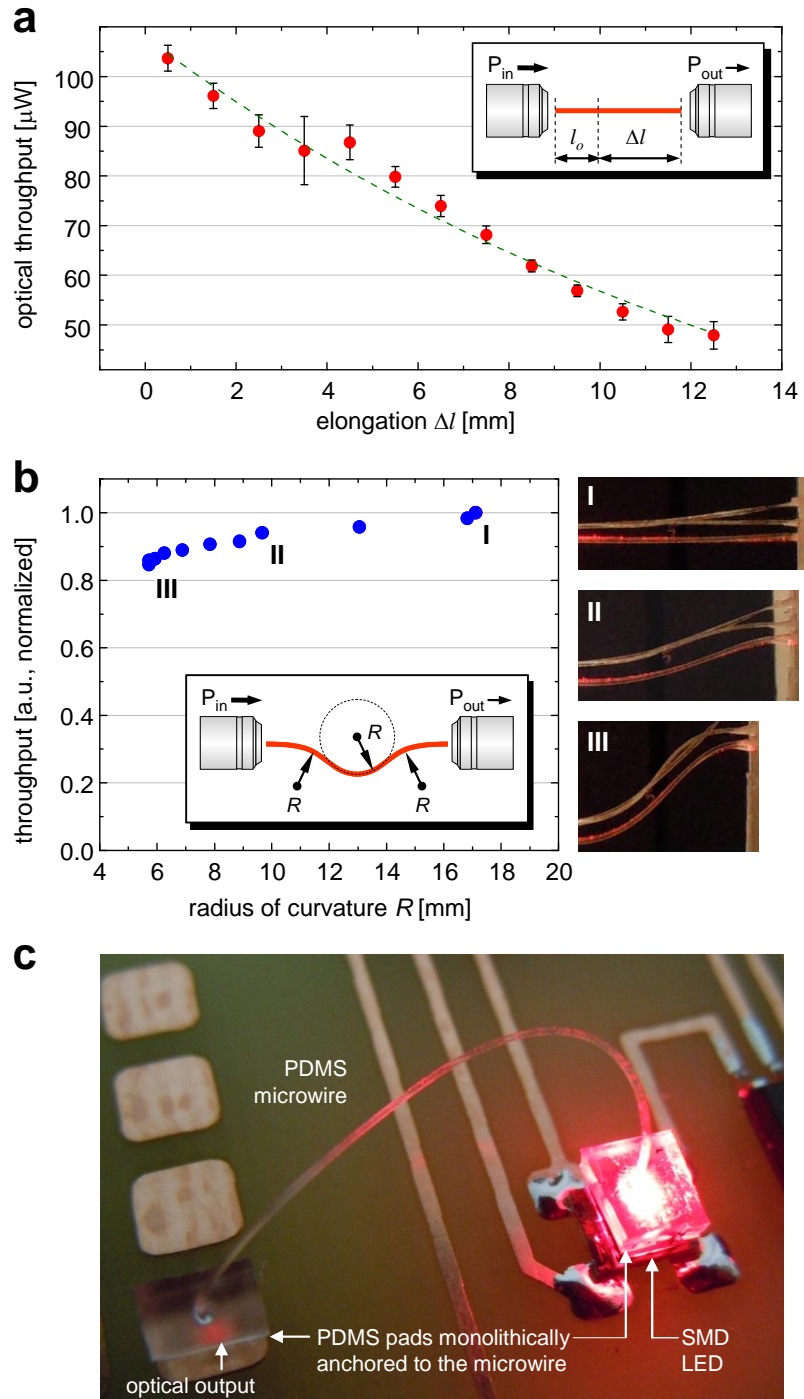


Figure 3.7 (a) Optical throughput measured as the length of the PDMS microwire is being increased by elongation  $\Delta l$ . The dotted curve represents the result of curve-fitting to exponential decay. (b) The optical throughput from a 2 cm-long, 184  $\mu\text{m}$ -diameter PDMS microwire as a function of the radius of curvature. The inset describes the experimental setup

and the parameters schematically. The insets also show the microwires bent with different  $R$  values. The red-colored microwires carry the HeNe light. (c) The same microwire was used as a jump-wire optically connecting a surface-mounted LED to a spot on the circuit board.

By installing the whole detection subsystem, consisting of the microwire output-end fixture, the collection objective lens, and the power meter head, on a linear translation stage, we could maintain the out-coupling condition regardless of the elongation  $\Delta l$ . Figure 3.7a shows the result of optical throughput measurements. The microwire under test was from a different batch which measures 188  $\mu\text{m}$  in diameter and approximately 8.2 mm in unstretched length  $l_0$ . As a function of elongation, the decrease in the throughput fit magnificently to the exponential decay function, well within the standard deviation obtained from four sets of measurements. The loss coefficient estimated from the fitting curve was 2.8 dB/cm, which corroborate the previous cut-back measurement result and also is a reasonable value for an unprotected multimode lightpipe with sub-mm diameter.

We also measured the microwire's bending loss using the setup shown schematically in the inset of Fig. 3.7b. Curvatures were induced at three points along a suspended microwire by reducing the distance between the input and output ends. We measured the changes in the out-coupled optical power and took one third of each value as the bending loss due to one curved section. The results were then normalized to the output level of a straight microwire (radius of curvature  $R = \infty$ ) and plotted in Fig. 3.7a as a function of  $R$ . It shows that the bending loss, which became noticeable when  $R$  reached 18 mm, was kept within 20% as  $R$  was reduced by a factor of three to 6 mm, which is approximately the radius of a semicircle with 2 cm in arc length. These results indicate that a 2 cm optical jump-wire, used as shown in Fig. 3.7c, will suffer less than 6 dB combined bending and propagation loss.

### 3.7 Conclusion

In conclusion, we proposed and demonstrated a new, lost-wax casting-based technique for fabricating elastomeric microwires that are monolithically anchored to external supporting structures at both ends. The technique, which literally *grows* the microwires, also allows the microwires to be aligned in the out-of-plane, surface-normal direction and facilitates their formation of patterned arrays. The PDMS microwires fabricated by the new technique, with their diameters and lengths ranging from 150 to 250  $\mu\text{m}$  and 2 to 20 mm, respectively, routinely withstood  $>400\%$  elongations with no degradation in surface smoothness noticeable from SEM scans. Some of the microwires withstood  $>70$  mN of pulling force while exhibiting the typical force-strain relation described by the Ogden model. The anchoring strength was certainly greater than the maximum pulling force withstood by each of the microwires. At 170  $\mu\text{m}$  in diameter, the doubly-anchored PDMS microwire exhibited 5.1 N/m in spring constant and 0.85  $\text{mJ}/\text{mm}^3$  in volume energy density, exhibiting potential as a MEMS energy storage element. Optical characterization also revealed that the PDMS microwires can function as elastic lightpipes optically connecting two points in miniaturized systems.

### 3.8 Acknowledgement

This work was supported by the National Science Foundation's CAREER award (#0954845).

### 3.9 References

- [1] Bergbreiter S, Mahajan D, and Pister K S J 2009 *J. Micromech. Microeng.* **19** 055009

- [2] Madangopal R, Khan Z A, and Agrawal S K 2006 *IEEE/ASME Trans. Mechatronics* **4** 433-438
- [3] Cho I K, Ryu J H, and Jeong M Y 2008 *Opt. Lett.* **33** 1881-1883
- [4] Monat C, Domachuk P, Grillet C, Collins M, Eggleton B J, Cronin-Golomb M, Mutzenich S, Mahmud T, Rosengarten G, and Mitchell A 2008 *Microfluid. Nanofluid.* **4** 81–95
- [5] Lee L P and Szema R 2005 *Science* **310** 1148-1150
- [6] Xing X, Wang Y, and Li B 2008 *Opt. Express* **16** 10815-10822
- [7] Tong L, Hu L, Zhang J, Qiu J, Yang Q, Lou J, Shen Y, He J, and Ye Z 2006 *Opt. Express* **14** 82-87
- [8] Harfenist S A, Cambron S D, Nelson E W, Berry S M, Isham A W, Crain M M, Walsh K M, Keynton R S, and Cohn R W 2004 *Nano Lett.* **4** 1931–1937
- [9] Spina G L, Stefanini C, Menciassi A, and Dario P 2005 *J. Micromech. Microeng.* **15** 1576
- [10] Nain A S, Phillippi J A, Sitti M, Mackerell J, Campbell P G, and Amon C 2008 *Small* **4** 1153–1159
- [11] Li D, Wang Y, and Xia Y 2003 *Nano Lett.* **3** 1167–1171
- [12] Teo W E and Rmakrishana S 2006 *Nanotechnology* **17** R89
- [13] Kessick R and Tepper G 2006 *Sens. Act. B* **117** 205-210
- [14] Pisignano D, Maruccio G, Mele E, Persano L, Benedetto F D, and Cingolani R 2005 *Appl. Phys. Lett.* **87** 123109
- [15] Jeong W, Kim J, Kim S, Lee S, Mensing G, and Beebe D J 2004 *Lab. Chip* **4** 576
- [16] Lee J and Kim J 2011 *Proc. IEEE Trans. Microelectromech. Syst. (MEMS)* 264-267

- [17] Engel J M, Chen J, Chang L, and Bullen D 2006 *IEEE/ASME J. Microelectromech. Syst.* **15** 729-735
- [18] Takeuchi S, Ziegler D, Yoshida Y, Mabuchi K, and Suzuki T 2005 *Lab. Chip* **5** 519-523
- [19] Yuan G, Wu X, Yoon Y K, and Allen M G 2005 *Proc. IEEE Microelectromech. Syst. (MEMS)* 411
- [20] Schaper C D 2004 *Proc. SPIE* **5374** 325
- [21] Wang S, Zeng C, Lai S, Juang Y J, Yang Y, and Lee L J 2005 *Adv. Mat.* **17** 1182-1186
- [22] Dharmatilleke S, Henderson H T, Bhansali S and Ahn C H 2004 *Proc. SPIE* **4177** 83
- [23] Vazquez G, Alvarez E, and Navaza J M 1995 *J. Chem. Eng. Data* **40** 611-614
- [24] Varga O H 1966, *Stress-Strain Behaviour of Elastic Materials*, Interscience, New York, 96
- [25] Pelrine R, Kornbluh R, Joseph J, Heydt R, Pei Q, and Chiba S 2000 *Materials Sci. Eng. C* **11** 89–100
- [26] Lin P and Yang S 2009 *Soft Matter* **5** 1011-1018
- [27] Lotters J C, Olthuis W, Veltink P H, and Bergveld P 1997 *J. Micromech. Microeng.* **7** 145-147
- [28] Armani D, Liu C, and Aluru N 1999 *Proc. 12th IEEE Int. Conf. MEMS*, 222-227
- [29] Eddington D T, Crone W C, and Beebe D J 2003 *Proceedings MicroTAS* 1089–1092
- [30] Kofod G and Sommer-Larsen P 2005 *Sens. Act. A* **122** 273-283
- [31] Ogden R W 1972 *Proc. R. Soc. Lond. A.* **326** 565-584

## CHAPTER 4. Compact range-tunable gas flow sensor utilizing stretchable optical microwire

Modified from a paper published in *Optics Letter*

Jiwon Lee and Jaeyoun Kim\*

### 4.1 Abstract

We present a new scheme for optical gas flow sensing utilizing stretchable microwires made of transparent elastomer PDMS. We utilized the elasticity of the PDMS microwire to miniaturize and simplify the sensor. By adjusting the tension of the microwire through mechanical stretching, we could widen and tune the sensing range as well. The experimental results exhibited affirmation of the predictions based on the fluid dynamic/optical model.

### 4.2 Introduction

Accurate and robust gas flow sensors are essential for a wide range of applications including biomedicine, process control, and environmental monitoring. Many physical effects have been exploited as transduction mechanisms. In particular, the last three decades have witnessed extensive utilizations of micro-electro-mechanical system (MEMS) technologies to miniaturize the sensors [1,2]. The sensitivity of those MEMS gas flow sensors is generally high at low flow rates (typically  $< 1$  SLM) but saturates rapidly as the flow rate increases [3]. This stimulates the development of new sensors with sensing ranges much wider than those of MEMS-based ones while maintaining their compactness.

In this letter, we present a new optical transduction scheme for realizing such a compact, wide-range gas flow sensor. Optical sensors are popular for their spark-free, electromagnetic interference-immune operations. Many optical gas flow sensors, primarily in fiber–optic forms, have been demonstrated [4-10]. But most of them rely on interferometric [4,5] or spectroscopic [6] interrogation systems which tend to be bulky and complex.

Interrogation by optical power measurement, which is much simpler, has been primarily employed by sensors relying on flow-induced bending of optical fibers [7-10]. Since the degree of bending yielded by glass or plastic optical fiber is small at flow rates of common interests, its impact had to be enhanced. Attaching a long section of sensing fiber to a bulky supporting structure has been a typical solution [7-9]. Others built a cantilever with a thinned fiber to convert bending into a misalignment in waveguide-to-waveguide coupling which results in a loss much greater than the bending loss itself [10]. These schemes, however, inevitably compromise the sensors' compactness and/or simplicity.

### 4.3 Fabrication Details

In our pursuit of compact, wide-range gas flow sensors, we also aimed to adopt the power measurement-based interrogation scheme without sacrificing its simplicity or size. The use of the stretchable optical microwire [11], a recent member of the stretchable optics [12,13], as the transducer, was the main enabling factor. Figures 4.1(a)-(e) show the steps to fabricate microwires with optically transparent elastomer poly(dimethylsiloxane) (PDMS) through lost–wax casting-based double replication of a metal wire. As shown in Figs. 4.1(e)-(g), microwires realized in this way are monolithically attached to external PDMS pads which facilitate their handling and utilization greatly. The site of monolithic attachment is optically

transparent and mechanically robust. We have routinely produced 5~20 mm-long, 80~120  $\mu\text{m}$  radius microwires. The PDMS microwires withstood  $>50$  mN pulling force, endured  $>400\%$  elongations, and exhibited  $< 3$  dB/cm propagation loss at 632.8 nm [11].

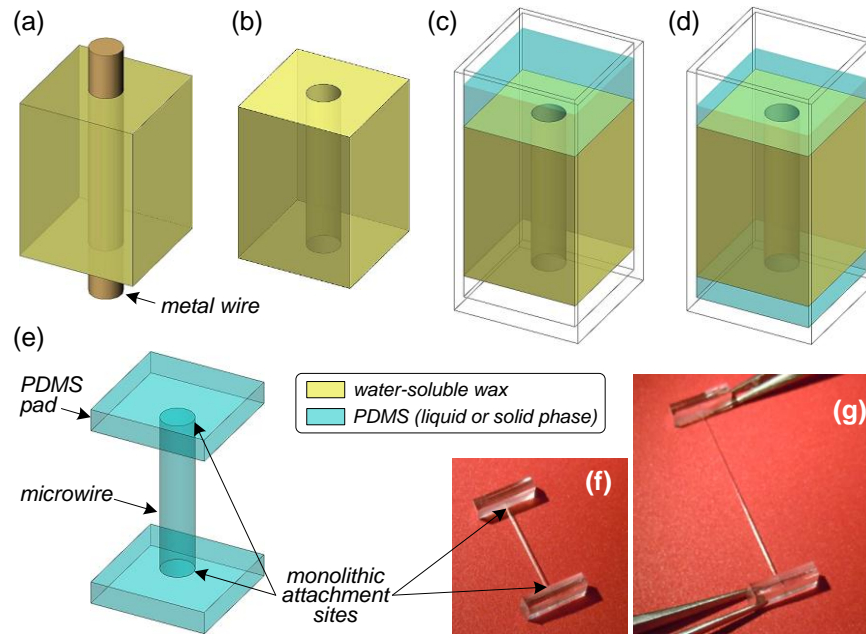


Figure 4.1 (a)-(e) PDMS microwire fabrication steps: (a)-(b) Preparation of a water-soluble wax mold with a cylindrical hole, (c)-(d) Inject liquid phase-PDMS through the hole, (e) After solidification, the microwire is released by water bath. (f) and (g) show images of a microwire (radius: 100  $\mu\text{m}$ , length: 1.2 cm), monolithically attached to handling pads at both ends, in its normal and 200% elongated states, respectively.

#### 4.4 Basic Principles

Figure 4.2 shows how we utilize the optical microwire for gas flow sensing. We first straighten the microwire to make it function as a lightpipe and expose it to gas flow. The resulting fluidic drag force bends the microwire and displaces the output beam from its original spot. Using an apertured screen, we can directly translate the center-to-center



displacement  $d$  into a decrease in the output optical power, which can be measured by an optical power meter. The elasticity of the microwire enables even a short ( $<1$  cm) section of it to yield sufficient bending for this type of direct detection. In contrast, optical fibers made of more rigid materials require special measures, such as splicing a section of single-mode fiber, for the detection of their bending, even if they were tightly stretched [14].

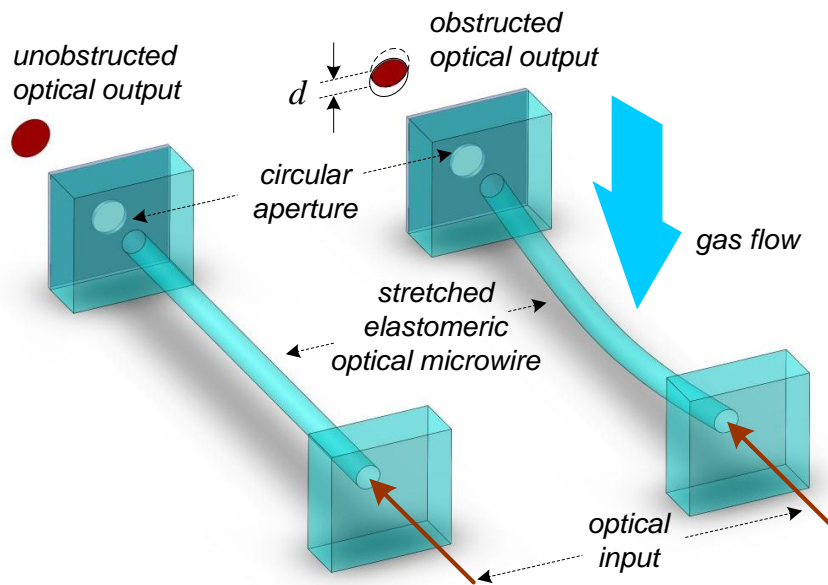


Figure 4.2 Operational principle of stretchable optical microwire-based gas flow sensing: The aperture translates the flow-induced bending into a decrease in the output power as a function of  $d$ , the center-to-center displacement between the beam and the aperture.

The tension of the microwire strongly affects the degree of bending. Since a wire under higher tension requires a stronger gas flow to yield the same degree of bending, we can expand the gas flow sensing range through additional stretching. The elasticity of PDMS and thinness of the microwire allows it to be stretched with only a few mN of force, facilitating the use of MEMS actuators.

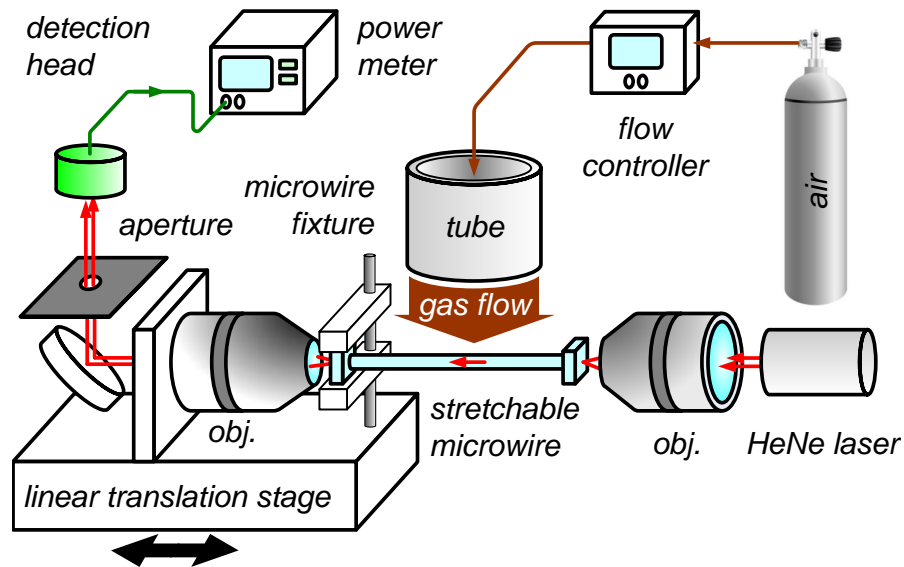


Figure 4.3 Experimental setup for gas flow sensing based on the stretchable optical microwire. The microwire is to be stretched by the linear translation stage on which the all the components from the fixture to the detection head are mounted.

The experimental setup for optical microwire-based gas flow sensing is shown schematically in Fig. 4.3. A 632.8 nm HeNe laser with 290  $\mu\text{W}$  output power was used as the light source. As the transducer, we used a 9 mm long, 188  $\mu\text{m}$  thick PDMS microwire attached to 1.5 mm thick PDMS pads at each end. Two 10 $\times$  microscope objectives were used for coupling the HeNe laser beam in and out of the microwire. While the input end of the microwire was permanently fixed in alignment with the in-coupling objective lens, the output end was mounted on a linear translation stage for variable stretching. In fact, to prevent the stretching process from affecting the out-coupling condition, we mounted all the components up to the detection head on the same translation stage. The radius of the aperture was 0.5 mm. The whole setup measures less than 15 cm in length. Most of the extent was taken up by

in- and out-coupling setup which can be replaced by microlenses formed directly on the PDMS pads for miniaturization in practical implementations.

As the source of gas flow, we used compressed dry air regulated 25 psi. The flow rate was varied between 0 to 5 SLM by a mass flow controller (Omega FMA5518). The gas flow was delivered to the experimental setup through a Teflon tube with 4.6 mm inner diameter. Using a 3-axis translation stage, we positioned the tube's center 9 mm above the microwire's midpoint. The corresponding gas flow velocity  $U$  was 0 ~ 5.1 m/s.

#### 4.5 Structural Characteristics

Figure 4.4(a) shows the measured optical power as a function of the gas flow rate and microwire elongation. We started from a sagged microwire and gradually stretched it while monitoring the output power. Once the microwire got completely straightened, the output power jumped abruptly and further elongation yielded little increase. We set that point as the zero-elongation point. For each flow rate, we sampled the output power for 120 seconds at 1 kHz and recorded the average value. After scanning the whole flow rate range, we changed the tension through elongation and repeated the measurement.

Figure 4.4(a) indicates that higher tension indeed widens the range of microwire-based gas flow sensing. If only the quasi-linear center portion of the response curve were concerned, stretching also shifts the sensing range. In our current setup, a -300, -200, and 200  $\mu\text{m}$  elongation shifts the center portion from 2.0~4.0 SLM to 1~1.5, 1.5~3.0, and 3.0~5.0 SLM, respectively.

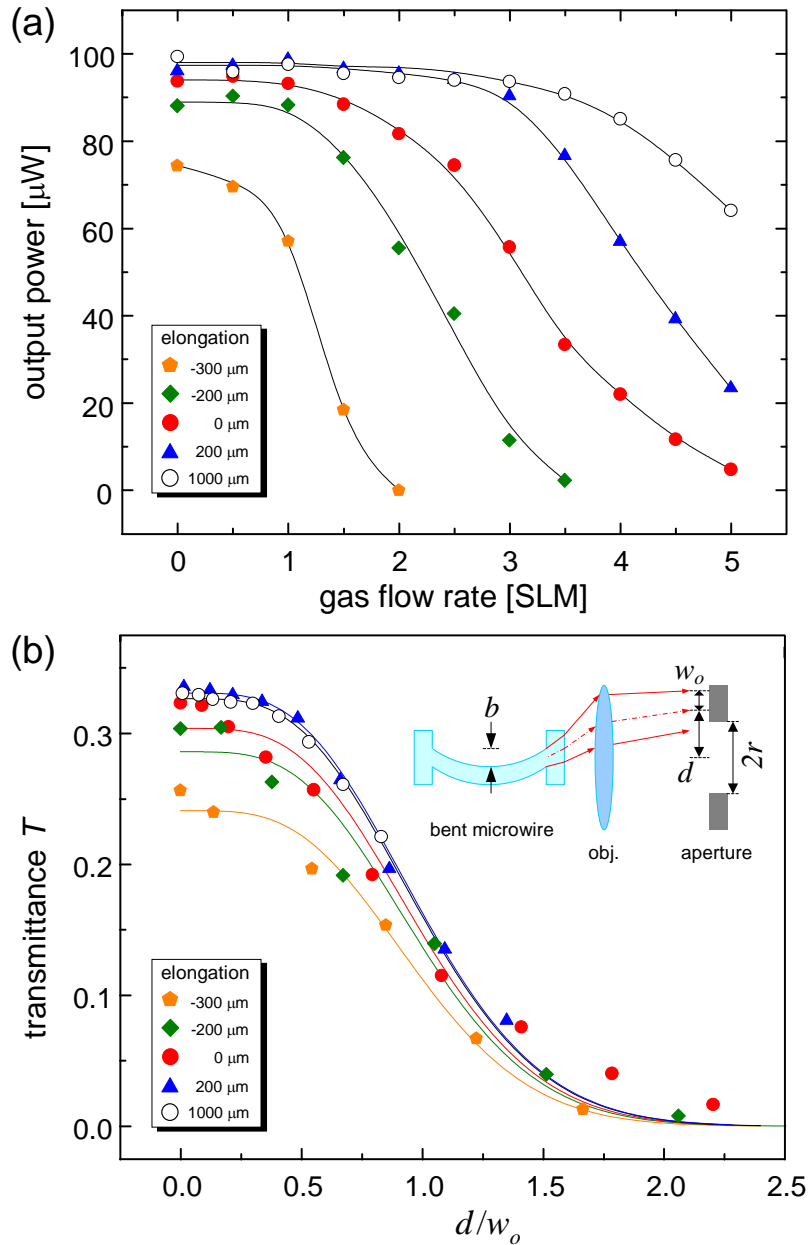


Figure 4.4 (a) Measured output power as a function of the gas flow rate and elongation. Spline-interpolation lines are added for visual aid. (b) The results of fitting the curves of (a) into Eq. 1. The inset shows the transducer model and parameters.

This range tunability has been highly sought after for multi-range sensing [15]. The response curve of the  $1000 \mu\text{m}$ -elongated microwire shows that the widening and shift can

also be saturated. The sensitivity obtained from the center portions of the first 4 response curves are 9.8, 5.5, 2.8, and 2.9 dB/SLM, which indicate that a trade-off exists between the sensing range and sensitivity.

#### 4.6 Experimental Results

By setting up a physical model and fitting the response curves to it, we can extract useful information for future applications of the optical microwire. The inset of Fig. 4.4(b) shows our model. The aperture transmittance  $T$  decreases as  $d$  increases. If the output beam took Gaussian intensity profile,  $T$  can be evaluated using

$$T = 1 - e^{-2(X^2+Y^2)} \sum_{n=0}^{\infty} \frac{2^n X^{2n}}{n!} \sum_{m=0}^n \frac{2^n Y^{2m}}{m!} \quad (1)$$

where  $X = d/w_o$ ,  $Y = r/w_o$ , and  $w_o$  and  $r$  are the radii of the output beam and the aperture, respectively [16].

To fit the response curves to Eq. 1, we must establish the relation between  $d$  and the elastic bending  $b$  which, in turn, is dependent on the gas flow velocity  $U$ . Since  $b$  leads to  $d$  through beam divergence, refraction at the PDMS-air interface, and imaging through an objective lens, quantifying their exact relation is difficult. Given the fact that most of the operations mentioned above are paraxial, we approximated  $d$  as a linear function of  $b$ . The proportionality factor was set to 4.5, the magnification of the collection optics. The relation between  $b$  and  $U$  can be obtained from  $b = F_D L^3 / (12\pi a^4 E)$  where  $L$  and  $a$  are the length and radius of the microwire and  $E$  is the Young's modulus. The fluidic drag force  $F_D = \frac{1}{2}\rho A U^2 C_D$

where  $A$  is the area of the microwire exposed to the flow,  $\rho$  the fluid density,  $C_D$  the drag coefficient of air, and  $U$  the flow velocity [10,17]. The value of  $E$ , however, can vary widely since it depends on many experimental parameters.

So we took only the skeletal part of the relation  $d \propto U^2/E$  and tried to fit all five curves to Eq. 1 using  $E$  and  $w_o$  as the variables. Since elongation less than 1 mm did not change the output beam size noticeably, we accepted only the  $E$  values which result in a consistent value for  $w_o$ . They are 0.91, 3.1, 7, 15, and 50 MPa for -300, -200, 0, 200 and 1000  $\mu\text{m}$  elongation, respectively. These values agree well with the  $E$  values measured independently [18]. The corresponding value of  $w_o$  was  $1.2 \pm 0.1$  mm which also agrees well with our observation. The agreement in Fig. 4.4(b) validates our transduction model consisting of Eq. 1 and the hypothesized quadratic relation  $d \propto U^2$ . The small discrepancies can be attributed to the deviation of the output profile from perfect Gaussian.

#### 4.7 Conclusion

In conclusion, we have experimentally demonstrated a new scheme for optical gas flow sensing using PDMS optical microwires as the transducer. The elasticity of the PDMS microwire not only allowed the use of simple, power measurement-based interrogation but also enabled widening and tuning of the sensing range through mechanical stretching. Since the present scheme keeps the probing light within the guiding structure throughout the sensing process, the stability of the sensor can be high. This scheme can also be extended to liquid flow sensing, and the chemical inertness of PDMS will greatly expand the scope of its application.

#### 4.8 Acknowledgement

This work is supported by NSF CAREER award (ECCS-0954845).

#### 4.9 References

- [1] N. T. Nguyen, "Micromachined flow sensors—a review," *Flow Meas. Instrument.* 8, 7–16 (1997).
- [2] Y.-H. Wang, C.-P. Chen, C.-M. Chang, C.-P. Lin, C.-H. Lin, L.-M. Fu and C.-Y. Lee, "MEMS-based gas flow sensors," *Microfluid. Nanofluid.* 6, 333–346 (2009).
- [3] P. Galambos and S. Braun, "Trends in MEMS fluid handling systems," *Fluid control*, 16, 24–26 (2010).
- [4] W. Peng, G. R. Pickrell, Z. Huang, J. Xu, D. W. Kim, B. Qi, and A. Wang, "Self-compensating fiber optic flow sensor system and its field applications," *Appl. Opt.* 43, 1752-1760 (2004).
- [5] Frazao, P. Caldas, F. M. Araujo, L. A. Ferreira, and J. L. Santos, "Optical flowmeter using a modal interferometer based on a single nonadiabatic fiber taper," *Opt. Lett.* 32, 1974-1976 (2007).
- [6] P. Caldas, P. A. S. Jorge, G. Rego, O. Frazao, J. L. Santos, L. A. Ferreira, and F. Araujo, "Fiber optic hot-wire flowmeter based on a metallic coated hybrid long period grating/fiber Bragg grating structure," *Appl. Opt.* 50, 2738-2743 (2011).
- [7] R. Philip-Chandy, P. J. Scully, and R. Morgan, "The design, development and performance characteristics of a fibre optic drag-force flow sensor," *Meas. Sci. Technol.* 11, N31-N35 (2000).

- [8] Vijayan, V. Thakare, R. N. Karekar, and R. C. Aiyer, "Optical fiber-based macrobend free air flow sensor using a hinge joint: A preliminary report," *Microw. Opt. Technol. Lett.* 50, 2543-2546 (2008).
- [9] R. P. Hu and X. G. Huang, "A simple fiber-optic flowmeter based on bending loss," *Sensors Journal, IEEE* 9, 1952-1955 (2009).
- [10] V. Lien and F. Vollmer, "Microfluidic flow rate detection based on integrated optical fiber cantilever," *Lab Chip.* 7, 1352-1356 (2007).
- [11] J. Lee and J. Kim, "Growing a patterned array of double-anchored elastomeric microwires using lost-wax casting," *Proc. IEEE 24th Annu. Int. Conf. Micro-Electro-Mechanical-Systems (Cancun, Mexico)*, 264-267 (2011).
- [12] N.-T. Huang, S.C. Truxal, Y.-C. Tung, A. Hsiao, S. Takayama, and K. Kurabayashi, "High-speed tuning of visible laser wavelength using a nanoimprinted grating optical tunable filter," *Appl. Phys. Lett.* 95, 211106 (2009).
- [13] V.J. Cadarso, A. Llobera, G. Villanueva, J.A. Plaza, J. Brugger, and C. Dominguez, "Mechanically tuneable microoptical structure based on PDMS," *Sens Act A*, 162, 260-266 (2010).
- [14] C. Fotsing-Djouwe, M. Gagné, J. Laurin, and R. Kashyap, "Optical fibre musical instruments making sense of the senseless," *J Mater Sci: Mater Electron* 20, 170-174 (2007).
- [15] N. Sabaté, J. Santander, L. Fonseca, I. Gràcia, and C. Cané, "Multi-range silicon micromachined flow sensor," *Sens. Act. A: Physical* 110, 282-288 (2004).
- [16] K. Uehara and H. Kikuchi, "Transmission of a Gaussian beam through a circular aperture," *Appl. Opt.* 25, 4514-4516 (1986).



- [17] *Polymer Testing*, W. Grellmann and S. Seidler, (Hanser, 2007).
- [18] F. Schneider, J. Draheim, R. Kamberger, and U. Wallrabe, "Process and material properties of polydimethylsiloxane (PDMS) for Optical MEMS," *Sens. Act. A*, 151, 95-99 (2009).

## CHAPTER 5. Sucrose-based fabrication of 3D-networked, cylindrical microfluidic channel for rapid-prototyping of lab-on-a-chip and vaso-mimetic device

Modified from a paper published in *Lab on a Chip*

Jiwon Lee, Jungwook Paek and Jaeyoun Kim,\*

### 5.1 Abstract

We present a new fabrication scheme for 3D-networked, cylindrical microfluidic (MF) channels based on shaping, bonding, and assembly of sucrose fibers. It is a simple, cleanroom-free, and environment-friendly method ideal for rapid-prototyping of lab-on-a-chip devices. Despite its simplicity, it can realize complex 3D MF channel architectures such as cylindrical tapers, internal loops, end-to-side junctions, tapered junctions, and stenosis. The last two will be of special use for generating vaso-mimetic MF structures. It also enables molding with polymers incompatible with high temperature processing.

### 5.2 Introduction

Lab-on-a-chip (LoC)'s rapidly expanding scope of application demands diverse changes in the architecture of microfluidic (MF) channels beyond their conventional forms with rectangular cross-sections and 2D, planar trajectories. Cylindrical MF channels<sup>1-10</sup> and 3D MF networks<sup>11-13</sup> have emerged as solutions and, along the efforts, the utility of MF channels that are cylindrical *and* 3D-networked got recognized as well. One eminent application is the vaso-mimetic LoC whose MF channels mimic biological vasculatures for tissue scaffolding<sup>14-16</sup> and controlled hemodynamic studies<sup>4,9,17-23</sup> in 3D environments.

Despite such application potential, the two architectures have been pursued largely in separation, leaving only a few schemes available for producing 3D-networked, cylindrical MF channels. In the omni-directional printing scheme<sup>24</sup>, cylindrical MF channels with 3D trajectories were fabricated by injecting cylindrical ink filaments that can be liquefied and drained upon solidifying the embedding material. Some schemes based on polymer molding of removable templates also achieved the dual goal using 3D-shapable cylindrical templates such as nylon<sup>25</sup>, metal<sup>26,27</sup>, or polymer<sup>28</sup> wires. Self-assembly of micro-tubules<sup>29</sup> and direct UV-writing<sup>30</sup> have also been demonstrated recently.

For a wider adoption of 3D-networked cylindrical MF channels, their fabrication scheme must be simple yet capable of realizing essential 3D MF architectures such as 3D-curved MF channels, MF channel junctions with a wide range of branching angle, and internally looped MF channels which start *and* end within the embedding polymer block. For vaso-mimetic LoCs, the MF channel junction must be physiologically realistic as well<sup>31,32</sup>. In particular, the MF junctions must be properly tapered to suppress unphysiological flow patterns that are detrimental to cell culture and hemodynamic modeling<sup>14</sup>.

Existing schemes exhibit limitations in these aspects. Schemes in which the template has to be physically pulled out require pre-swelling of the embedding polymer block, a process prone to deform the pattern<sup>25,26</sup>. Moreover, such schemes cannot produce internally looped MF channels. Thermally dissolvable metal wires tend to produce channels with initial diameter  $> 300 \mu\text{m}$ <sup>27</sup>. Only recently was the channel size issue addressed by casting thermally dissolvable polymer into a very thin fiber form<sup>28</sup>. Most template-based schemes are also very limited in their ability to form a proper 3D MF junction in which the center of one cylindrical channel's cross-section meets the side of the other channel at its midline. Forming

such a junction needs end-to-side bonding of two cylindrical templates. With the template materials not providing effective bonding methods, end-to-side junctions have been made by thermal<sup>25,28</sup> or mechanical<sup>26</sup> fusion of two simply over-stacked templates. Such processes, however, hamper the formation of predictable junction shapes, let alone the tapered ones required for vaso-mimetic LoCs. Omni-directional printing<sup>24</sup>, self-assembly<sup>29</sup>, and UV-writing<sup>30</sup> schemes are more promising in these aspects, but the accompanying demands for specialized instruments and materials huddle their wide adoption.

In this paper, we describe a new fabrication scheme for 3D-networked, cylindrical MF channels which addresses all issues stated above. Our scheme allows facile realizations of highly curved 3D MF channel trajectories, proper MF junctions, and internally looped MF channels. The diameter of the MF channels can be well below 100  $\mu\text{m}$ . It also allows the formation of tapered junctions and locally dented MF channels, which will especially benefit vaso-mimetic applications. Utilizing only water-based, low-temperature processes, our scheme is ideal for rapid prototyping of LoCs without fume-hoods or clean room facilities.

The main enabling factor is the use of sucrose as the template material. Sucrose is a readily available material that can be drawn into thin cylindrical fibers at low temperatures. The resulting fibers display mechanical and surface characteristics suitable for handling, shaping, and formation of transparent MF channels. Removal of the sucrose fiber requires only warm water, allowing fabrication of complex MF networks in fume-hood-free settings. It also permits the use of polymers incompatible with strong etchants and/or high molding temperature.

These beneficial features of sucrose as a sacrificial template material have been exploited for LoC fabrication in two different ways. Bellan *et al.* fabricated 3D artificial vascular

structures by melt-spinning random sugar fiber networks and then molding them with curable polymer<sup>33</sup>. On the other hand, Li *et al.* fabricated bundles of poly-(L-lactic acid) (PLLA) tubules by coating sucrose fibers with PLLA and then dissolving the fibers, for eventual use as MF nerve scaffolds<sup>34</sup>. However, there has been no explicit report on shaping/assembly of the sucrose fibers to form 3D networks, as Esser-Kahn *et al.* have done with polylactide (PLA) fibers to make 3D vasculated structures<sup>28</sup>. Unlike sucrose, however, PLA template removal and fusion-based junction formation require 200~280°C.

Our scheme distinguishes itself from other sucrose-based ones by providing specific techniques to shape, assemble, and bond the sucrose fibers. They allow us to build *pre-designed*, rather than random<sup>33</sup> or monotonically tubular<sup>34</sup>, 3D networks of cylindrical MF channels, which will eventually lead to vaso-mimetic LoCs.

## 5.3 Materials and methods

### 5.3.1 Pulling and shaping of sucrose fiber templates

Steps for sucrose fiber fabrication are described in Figs. 5.1a-b. Sucrose (S5-500, Fisher) was melted at 200°C for 10 min. Then we decreased the temperature to 125°C and waited for 20 minutes at which the sucrose viscosity became optimal. While maintaining the temperature, we pulled sucrose fibers with a cylindrical rod moving at 0.1~26 cm/s. The pulling speed mainly controlled the sucrose fiber diameter. The diameter of the pulling rod was also important. For sucrose fibers with diameter < 80 µm, we used a 125 µm-diameter glass fiber (SMF-28, Corning). For thicker ones, we used un-jacketed SMF-28 (900 µm in diameter).

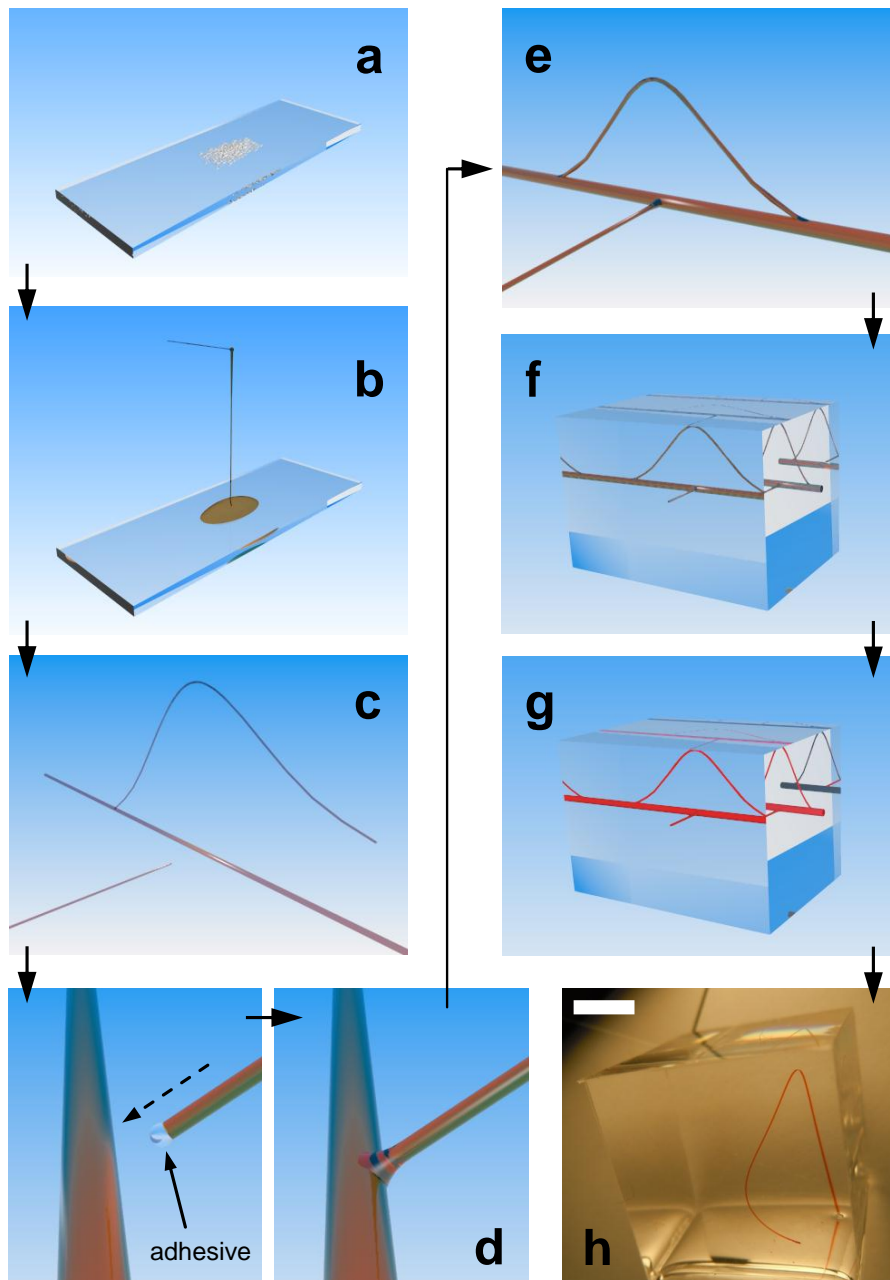


Figure 5.1 Schematic outline of the sucrose-based rapid-prototyping process: (a) We melted sucrose and (b) pulled fibers which can be (c) shaped and (d) bonded with water-based adhesives (e) to form a template assembly. (f) Then we immersed it in liquid-phase PDMS. (g) Upon curing, the template was removed from the water bath. For visualization, we filled the channels with dye. (h) A 3D MF channel in PDMS (scale bar: 5 mm).

We routinely produced highly uniform fibers with  $< \pm 5 \mu\text{m}$  deviation in diameter. The fibers were examined with optical (E-Zoom6, Edmund) and atomic force (Veeco) microscopes. We consistently obtained fibers with their diameters ranging from 30 to 900  $\mu\text{m}$ . Diameter  $< 30 \mu\text{m}$  led to handling difficulties. The upper limit was only set by the availability of adequate pulling rods and the ability to maintain a constant temperature over its facet. The fibers were then shaped in preparation for the assembly, as shown in Fig. 5.1c. By controlling the pulling conditions, we could taper the fibers as well. More details on the shaping and tapering of the sucrose fibers can be found in Supplementary Information.

### 5.3.2 Sucrose template bonding, assembly, and replication

Junctions were made by bonding one end of a sucrose fiber to the side of another. We used two methods, both based on the high water solubility of sucrose. In the first, we used steam to provide moisture and heat simultaneously. The two areas to be bonded were exposed to water vapor at  $90^\circ\text{C}$  for 3 seconds and were then attached. Subsequently, the junction was annealed by a few seconds of extra vapor exposure. In the second method, we used sucrose mixed with  $90^\circ\text{C}$  water at 2:3 weight-ratio as the adhesive as shown in Fig. 5.1d. The amount of required adhesive depends on the junction area. For instance, we applied 0.4 nL adhesive to bond 100  $\mu\text{m}$ -diameter fibers. We added water continuously to maintain the adhesive composition. While requiring an additional step, this method enables a stronger bonding and a wider junction area. Furthermore, this method can produce tapered junctions, contributing critically to the vaso-mimetic effort. Further details on the assembly process of complex 3D MF networks and their replication (Figs. 5.1f and g) with PDMS and

polyurethane-based optical polymer are in Supplementary Information. Figure 5.1h shows one 3D MF network made within a PDMS cube.

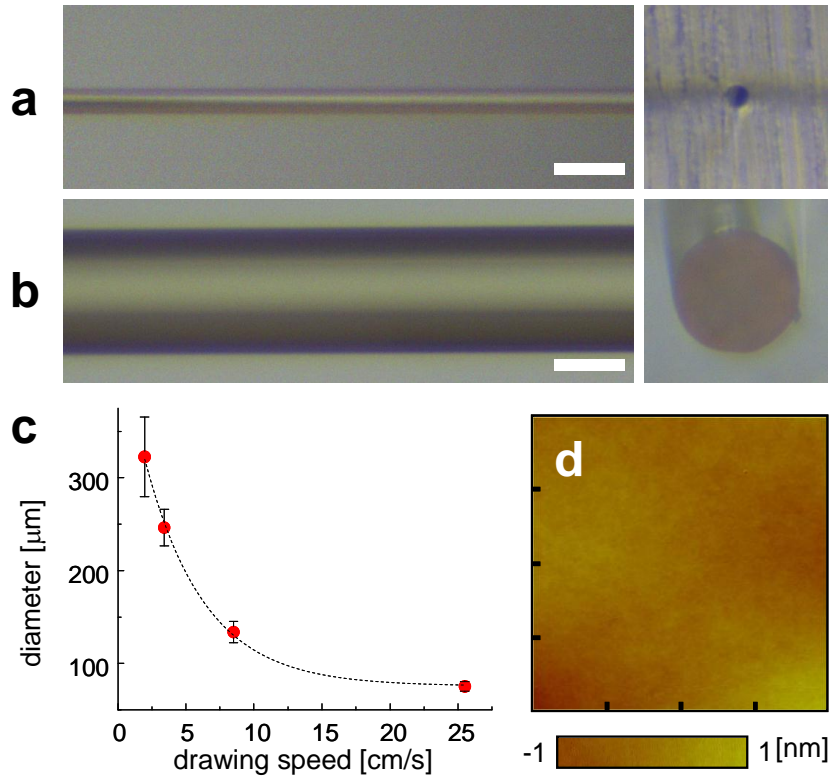


Figure 5.2 Optical microscope images of sucrose templates pulled at (a) 25.6 and (b) 2.0 cm/s in side and cross-section views. Scale bars: 100 μm. (c) The template diameter as a function of the pulling speed. The dotted curve represents an exponential decay. (d) An AFM scan image over a  $4 \times 4 \mu\text{m}^2$  area on a sucrose template.

## 5.4 Results and discussion

### 5.4.1 Physical characteristics of sucrose templates

Figures 5.2a and 5.2b show the microscope images of the sucrose fibers pulled at 25.6 and 2.0 cm/s in side and cross-sectional views. The graph in Fig. 5.2c also presents statistics obtained from five measurements. It indicates that thinner fibers pulled at higher speeds



exhibit better repeatability in diameter, probably due to shorter exposure to environmental disturbances. The curve-fitting result shows that the diameter and pulling speed are related through an exponential decay function. Within the observed range of pulling speed, the sucrose templates reveal excellent cross-section circularity. More details on physical and surface characteristics of the fibers are in Supplementary Information.

#### 5.4.2 MF junction formation

The water-dissolvable nature of sucrose facilitates the realization of MF channel junctions greatly. Two template bonding methods were described in the previous section. Figures 5.3a and 5.3b are the microscope images of two steam-bonded sucrose templates (633 and 220  $\mu\text{m}$  thick) in the side and bird's-eye view, respectively. It is clear that the cross-sectional center of the thinner template meets the side of the thicker one at its midline, forming a proper end-to-side junction. The steam-bonding is also effective for attaching sucrose templates with greatly dissimilar diameters at a wide range of branching angle. Figure 5.3c shows a junction between sucrose templates with 594 and 63  $\mu\text{m}$  in diameters. Even though the two met at a near-grazing angle, they formed a mechanically robust junction that can withstand subsequent manual handling. Figure 5.3d shows the PDMS MF channel branch molded from the template in Fig. 5.3c. The flow of red dye clearly confirms proper MF channel branching. The branching point in Fig. 5.3d is actually located on the far side of the main channel and the transparency attests to the exceptional surface quality of the molded channel.

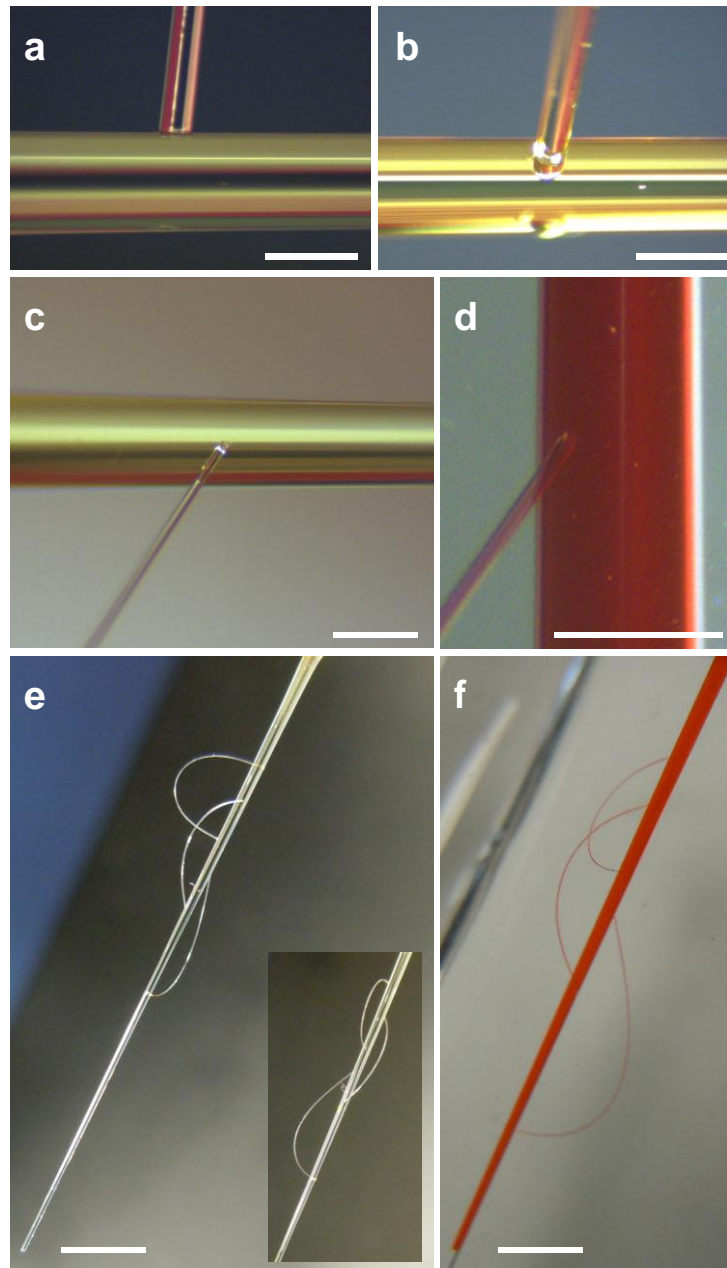


Figure 5.3 An end-to-side junction formed between two sucrose templates in (a) side and (b) bird's-eye view. (c) Steam-bonding is also effective between templates with greatly dissimilar diameters. (d) A MF channel branch PDMS-replicated from (c). The junction is located on the far side but clearly visible, confirming the transparency of the MF channel. (e) A 3D assembly of three internally looped templates to a cylindrically tapered backbone. No loop is in the same plane with another. (f) A 3D MF network made with (e). Scale bars: (a)-(d) 600  $\mu\text{m}$ , (e)-(f) 5 mm.

#### 5.4.3 3D MF channels trajectories and internal looping

The highly curved templates, such as the ones shown in Fig. 5.1e, can be bonded to other templates to obtain more complex 3D MF networks. Thanks to the easy, water-based dissolution process for sucrose, the templates can take more complex forms such as internal loops. Figure 3e shows a template assembly with 3 internally looped, 68  $\mu\text{m}$ -thick branches steam-bonded to a backbone. The backbone itself is tapered with its diameter changing from 622 to 237  $\mu\text{m}$  over 2.5 cm ( $0.44^\circ$  taper angle), achieving another important architecture in 3D. Details of tapering is in Supplementary Information. Figure 5.3e and its inset, a slightly rotated view, clearly show that none of the loops are in the same plane, forming a completely 3D network. The minimum radius of curvature was 1.43 mm. Figure 5.3f shows the flow of red dye through the multi-branching network molded from the template with PDMS, affirming the integrity of the MF network.

#### 5.4.4 Vaso-mimetic architectures: tapered junctions and stenosis

Sucrose-based scheme's other important feature is its ability to realize templates with their shapes varying rapidly in the axial direction. Figure 5.4a shows one example: a junction between two templates (387 and 61  $\mu\text{m}$  in diameter) made with the second, adhesive-based bonding method. By controlling the volume of liquid adhesive and the speed of its application, a wide variety of junction shapes can be realized. Due to the total water-solubility of the adhesive itself, the PDMS-molded channels replicate the junction shape with high fidelity, as shown in Fig. 5.4b. As mentioned in the introduction, this tapered junction will contribute greatly to the completion/attainment of vaso-mimetic LoCs. As another example of axially modifying the template, we made a smooth dent (687 and 178  $\mu\text{m}$  in

length and height, respectively) to a 436  $\mu\text{m}$ -thick sucrose template using the material's low-temperature deformability. Figure 5.4c shows that the PDMS-molded channel replicated the dent shown in the inset. Such a localized deformation in a 3D-curved cylindrical microfluidic channel will function as an ideal mimicry for studying the impact of stenosis on blood cells' hydrodynamic behaviors.

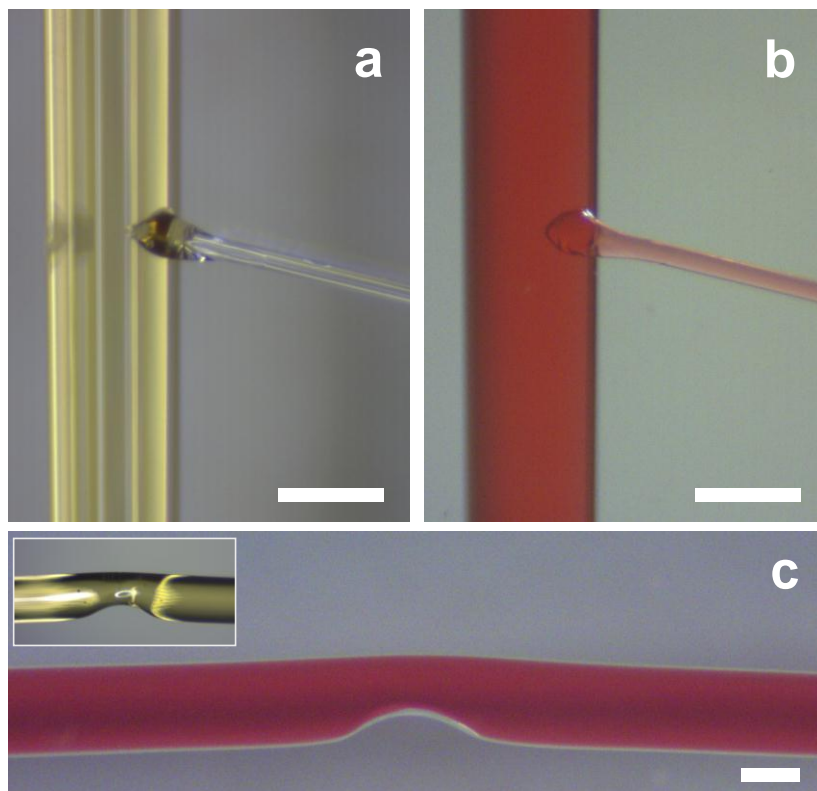


Figure 5.4 Vaso-mimetic MF architectures: (a) A tapered junction between two sucrose templates bonded with water-based adhesive. (b) A PDMS MF channel molded from (a) with red dye flowing through the branch. (c) A stenosis-like structure formed by localized thermal deformation of the sucrose template (inset) and its PDMS molding. Scale bars: 300  $\mu\text{m}$ .

## 5.5 Conclusions

In conclusion, we have demonstrated a new fabrication scheme for 3D-networked, cylindrical MF channels based on the shaping, bonding, and assembly of sucrose fibers. It is a simple and fast method requiring no cleanroom facility or fume-hoods. Its total reliance on sugar and water also makes the fabrication process very environment friendly. Despite its simplicity, our scheme can produce complex, pre-designed 3D networks, rather than the random or monotonic ones realized with existing schemes. The list of 3D MF channel architectures uniquely obtainable with our scheme includes: cylindrical tapers, internal looping, end-to-side junctions, tapered junctions, and local stenosis. The last two will especially benefit vaso-mimetic efforts, hemodynamic studies, and 3D tissue scaffolding. Finally, the low temperature required to dissolve the template will allow molding with polymers incompatible with high processing temperature, such as polyurethane (PU).

## 5.6 Acknowledgements

This work was supported through National Science Foundation grants ECCS-1147413 and ECCS-0954845.

## 5.7 Notes and references

- [1] M. Abdelgawad, C. Wu, W.-Y. Chien, W. R. Geddie, M. A. S. Jewett, and Y. Sun, *Lab Chip*, 2011, **11**, 545.
- [2] S. H. Lee, D. H. Kang, H. N. Kim, and K. Y. Suh, *Lab Chip*, 2010, **10**, 3300.
- [3] A. Asthana, K.-O. Kim, J. Perumal, D.-M. Kim, and D.-P. Kim, *Lab Chip*, 2009, **9**, 1138.

- [4] L. K. Fiddes, N. Raz, S. Sriganapalan, E. Tumarkan, C. A. Simmons, A. R. Wheeler, E. Kumacheva, *Biomaterials*, 2010, **31**, 3459.
- [5] M. E. Wilson, N. Kota, Y. Kim, Y. Wang, D. B. Stolz, P. R. LeDuc, and O. B. Ozdoganlar, *Lab Chip*, 2011, **11**, 1550.
- [6] H. Perry, C. Greiner, I. Georgakoudi, M. Cronin-Golomb, and F. G. Omenetto, *Rev. Sci. Instrum.* 2007, **78**, 044302.
- [7] A. P. Dahlin, S. K. Bergstrom, P. E. Andren, K. E. Markides, and J. Bergquist, *Anal. Chem*, 2005, **77**, 5356-5363.
- [8] K. Lee, C. Kim, K. S. Shin, J. W. Lee, B.-K. Ju, T. S. Kim, S.-K. Lee, and J. Y. Kang, *J. Micromech. Microeng.* 2007, **17**, 1533-1541.
- [9] R. Lima, M. S. N. Oliveira, T. Ishikawa, H. Kaji, S. Tanaka, M. Nishizawa, and T. Yamaguchi, *Biofabrication*, 2009, **1**, 035005.
- [10] E. Kang, S.-J. Shin, K. H. Lee, and S.-H. Lee, *Lab Chip*, 2010, **10**, 1856-1861.
- [11] H. Wu, T. W. Odom, D. T. Chiu, and G. M. Whitesides, *J. Am. Chem. Soc.* 2012, **125**, 554-559.
- [12] Y. Luo and R. N. Zare, *Lab Chip*, 2008, **8**, 1688.
- [13] K.-S. Yun and E. Yoon, *Lab Chip*, 2008, **8**, 245.
- [14] J. T. Borenstein, M. M. Tupper, P. J. Mack, E. J. Weinberg, A. S. Khalil, J. Hsiao, and G. Garcia-Cardena, *Biomedical Microdevices*, 2010, **12**, 71-79.
- [15] J. T. Borenstein and G. Vunjak-Novakovic, *IEEE Pulse*, 2011, **2**, 28.
- [16] E. C. Novosel, C. Kleinhans, and P. J. Kluger, *Advanced Drug Delivery Reviews*, 2011, **63**, 300-311.

- [17] J. Hanzlik, E. Cretekos, and K. A. Lamkin-Kennard, *Journal of Bionic Engineering*, 2008, **5**, 317-327.
- [18] A. D. van der Meer, A. A. Poot, M. H. G. Duits, J. Feijen, and I. Vermes, *J. Biomed. Biotech.* 2009, **2009**, Article ID 823148
- [19] B. Prabhakarandian, M.-C. Shen, K. Pant, and M. F. Kiani, *Microvascular Research*, 2011, **82**, 210-220.
- [20] M. K. Runyon, C. J. Kastrup, B. L. Johnson-Kerner, T. G. Van Ha, and R. F. Ismagilov, *J. Am. Chem. Soc.* 2008, **130**, 3458-3464.
- [21] S. S. Shevkoplyas, S. C. Gifford, T. Yoshida, and M. W. Bitensky, *Microvascular Research*, 2003, **65**, 132-136.
- [22] X. Yang, O. Forouzan, J. M. Burns, and S. S. Shevkoplyas, *Lab Chip*, 2011, **11**, 3231-3240.
- [23] O. Forouzan, J. M. Burns, J. L. Robichaux, W. L. Murfee, and S. S. Shevkoplyas, *Lab Chip*, 2011, **11**, 1924-1932.
- [24] W. Wu, A. DeConinck, and J. A. Lewis, *Advanced Materials*, 2011, **23**, H178-H183.
- [25] M. K. S. Verma, A. Majumder, and A. Ghatak, *Langmuir*, 2006, **22**, 10291.
- [26] Y. Jia, J. Jiang, X. Ma, Y. Li, H. Huang, K. Cai, S. Cai, and Y. Wu, *Chinese Science Bulletin*, 2008, **53**, 3928-3936.
- [27] S.-H. Song, C.-K. Lee, T.-J. Kim, I. Shin, S.-C. Jun, and H.-I. Jung, *Microfluidics and Nanofluidics*, 2010, **9**, 533-540.
- [28] A. P. Esser-Kahn, P. R. Thakre, H. Dong, J. F. Patrick, V. K. Vlasko-Vlasov, N. R. Sottos, J. S. Moore, and S. R. White, *Advanced Materials*, 2011, **23**, 3654-3658.

- [29] Y. Du, M. Ghodousi, H. Qi, N. Haas, W. Xiao, and A. Khademhosseini, *Biotech. Bioengineering*, 2011, **108**, 1693-1703.
- [30] C. Xia and N. X. Fang, *Biomedical Microdevices*, 2009, **11**, 1309.
- [31] J. M. Rosano, N. Tousi, R. C. Scott, B. Krynska, V. Rizzo, B. Prabhakarandian, K. Pant, S. Sundaram, and M. F. Kiani, *Biomed Microdevices*, 2009, **11**, 1051-1057.
- [32] S. Zhao, X. Xu, A. Hughes, S. Thom, A. Stanton, B. Ariff, and Q. Long, *Journal of Biomechanics*, 2000, **33**, 975-984.
- [33] L. M. Bellan, S. P. Singh, P. W. Henderson, T. J. Porri, H. G. Craighead, and J. A. Spector, *Soft Matter*, 2009, **5**, 1354-1357.
- [34] J. Li, T. A. Rickett, and R. Shi, *Langmuir*, 2008, **25**, 1813-1817.



## CHAPTER 6. Conclusion and Future Aspects

By conducting reviews of current interests in bioengineering, I realized that microfluidics and polymer-based MEMS devices play significant roles in advancing the fields. In particular, the development of platform technologies, which enable the fabrication of microscale systems with ease at a low cost, seems indispensable. Polymer-based technologies help reduce the price of microscale fabrication. It is also essential for mimicking biological systems in nature which are inherently made with soft materials. Simple yet elegant structures found in nature have provided endless sources of inspiration, prompting many great scientific and engineering advances. In this work, I developed four major platform technologies to contribute to bioengineering.

First, I studied a microscale optofluidic waveguiding scheme and its potential in functioning as an optical sensor. An optical sensor is preferred for its EMI-free nature in biomedical applications. By utilizing theoretical and numerical methods, anti-resonance reflection-based light confinement was proposed and validated. Specifically, the optimum confinement conditions for the proposed ML/SL-ARROW design have been investigated. Upon proper selection of the parameters, the propagation lengths of light waveguiding could be as long as 6 to 10 cm, which is useful for sensing. Moreover, the wavelength scan performed with the structure (Fig. 2.5c), proves its potential as a FL biosensor.

As an effort to develop a low-cost, simple sensing technology, I also studied bio-inspired polymer microwires. The polymer MEMS structure can be utilized as optical waveguides in the same way that the deep-sea amphipod, sensors, or actuators do. I devised a simple fabrication method using elastomer molding, which is a soft lithography method. Since only poly(dimethylsiloxane) (PDMS), water soluble wax, and the stainless-steel-wire templates

were used, the method was also very cost-effective. Using the method, we obtained a 10 x 10 array of 150  $\mu\text{m}$ -diameter polymer wires, which can be elongated more than 300% repeatedly. The surface quality tested by SEM and AFM especially proves its smoothness in microscale. With four different diameter microwires, tensile strength was also tested. The force-strain curve computed with the Ogden model shows that microwires thicker than 200  $\mu\text{m}$  in diameter can withstand force higher than 70 mN.

As an extension of the previous work, I developed a bio-inspired gas flow sensor using the PDMS microwire. A 100  $\mu\text{m}$ -diameter PDMS wire was used as the transducer which is optically transparent and tunable. By fixing the input end and laterally changing the output end of the PDMS transducer, I could change the tension. The sensing range was altered by tension applied to the polymer transducer. Fig. 4.4b illustrates the range tunability scan for several elongated stages and also proves the flow rate modification from 1 to 4 SLM over 500 $\mu\text{m}$ -elongation. The sensitivity measured for high elasticity was 9.8dB/SLM at 1 cm.

The last part established another fabrication technique based on elastomer molding of a bio-compatible material, sucrose, as a solution to generate microfluidic channels imitating vasculatures complete with circular cross sections and 3D assemblies. Thanks to the sucrose and its humid/temperature deformability, microscale (smallest 20  $\mu\text{m}$  to several hundred micrometers) structures were fabricated and assembled. The smooth surface of the pulled sucrose was confirmed with AFM over 16  $\mu\text{m}^2$  of several randomly chosen areas. This platform technology also provided tapered, stenosis-like, and internally looping structures, which will be useful for biomedical studies.

In summary, I have actively sought bio-inspired solutions to well-known problems in bioengineering, emphasizing ease of fabrication, low cost, and miniaturization. Through the

platform technologies studied, the research group gained ample experience for developing more complicated sensors. I am positive that we would achieve more by combining the optical components and microfluidics we had developed as well as through learning from nature more proactively. It also seems that each of the platform technologies can be further improved. For instance, the optofluidic sensor can be fabricated with MEMS and tested; polymer wire actuators can be thinner down by utilizing pulling and temperature control; and endothelial cells should be grown inside the vasomimetic channels to perform actual cell mechanics or vascular studies.